Impact of the Juan Fernandez ridge on the Pampean flat subduction inferred from full waveform inversion

Yajian Gao[1], Xiaohui Yuan[1], Benjamin Heit[1], Frederik Tilmann[1], Dirk Philip van Herwaarden[2], Solvi Thrastarson[2], Andreas Fichtner[2], and Bernd Dieter Schurr[3]

[1]Helmholtz Centre Potsdam - German Research Centre for Geosciences (GFZ)
[2]ETH Zurich, Switzerland
[3]Deutsches GeoForschungsZentrum GFZ

November 23, 2022

Abstract

A new seismic velocity model for the south Central Andes is derived from full waveform inversion, covering the Pampean flat and adjacent Payenia steep subduction segments. Strong focused crustal low-velocity anomalies indicate partial melts in the Payenia segment along the volcanic arc, whereas weaker low-velocity anomalies covering a wide zone in Pampean possibly indicates remnant melts in the past. Thinning and tearing of the flat Nazca slab below the Pampean is inferred by gaps in the high-velocity slab along the inland projection of the Juan-Fernandez-Ridge. A high-velocity anomaly in the upper mantle below the flat slab is interpreted as a relic Nazca slab segment, which indicates an earlier slab break-off during the flattening process, triggered by the buoyancy of the Juan-Fernandez-Ridge. In Payenia, large-scale low-velocity anomalies atop and below the re-steepened Nazca slab are associated with the re-opening of the mantle wedge and sub-slab asthenospheric flow, respectively.

Impact of the Juan Fernandez ridge on the Pampean flat subduction inferred from full waveform inversion

Yajian Gao[1,2], Xiaohui Yuan[1], Benjamin Heit[1], Frederik Tilmann[1,2], Dirk-Philip van Herwaarden[3], Solvi Thrastarson[3], Andreas Fichtner[3], Bernd Schurr[1]

[1]GFZ German Research Centre for Geosciences, Potsdam, Germany
[2]Freie Universität Berlin, Berlin, Germany
[3]ETH Zürich, Zürich, Switzerland

Key Points:

- A new seismic model for the crust and upper mantle beneath central Chile and western Argentina is presented.
- Thinning and tearing within the Pampean flat slab is detected along the inland projection of the Juan Fernandez Ridge.
- A relic slab is imaged beneath the Pampean flat slab, reflecting slab break-off during the flattening process.

Corresponding author: Yajian Gao, yjgao@gfz-potsdam.de

Abstract

A new seismic velocity model for the south Central Andes is derived from full waveform inversion, covering the Pampean flat and adjacent Payenia steep subduction segments. Strong focused crustal low-velocity anomalies indicate partial melts in the Payenia segment along the volcanic arc, whereas weaker low-velocity anomalies covering a wide zone in Pampean possibly indicates remnant melts in the past. Thinning and tearing of the flat Nazca slab below the Pampean is inferred by gaps in the high-velocity slab along the inland projection of the Juan-Fernandez-Ridge. A high-velocity anomaly in the upper mantle below the flat slab is interpreted as a relic Nazca slab segment, which indicates an earlier slab break-off during the flattening process, triggered by the buoyancy of the Juan-Fernandez-Ridge. In Payenia, large-scale low-velocity anomalies atop and below the re-steepened Nazca slab are associated with the re-opening of the mantle wedge and sub-slab asthenospheric flow, respectively.

Plain Language Summary

Taking advantage of the abundant information recorded in seismic waveforms, we imaged the seismic structure of the crust and upper mantle beneath central Chile and western Argentina, where the oceanic Nazca slab is subducting beneath the South American plate. The Nazca plate is almost flat in the north of the study area below the Pampean region, where the Juan Fernandez seamount ridge is attached on the subducting Nazca slab. The slab steepens again in the south in the Payenia region. Our model reveals pronounced low-velocity anomalies in the middle of the Pampean flat slab along the inland projection of the Juan Fernandez Ridge, indicating that the Pampean flat slab is thinned or even torn apart. A high-velocity anomaly is imaged beneath the flat slab, representing a former slab segment that was broken off during the slab flattening process and was overridden by the advancing young slab. Our model suggests a causal relationship between the oceanic ridge subduction and the flat slab formation. In the Payenia region, the slab re-steepening resulted in the re-establishment of the mantle wedge and induced subslab asthenospheric flow, which are characterized by low-velocity anomalies in the model.

1 Introduction

The causes and consequences of flat subduction along the South American western margin are vigorously debated (e.g., Gutscher et al., 2000; Ramos & Folguera, 2009). Two prominent on-going flat subduction segments beneath the Andes are the Peruvian and Pampean flat subduction zones, north and south of the conspicuous kink in the South American coastline respectively. They have been documented based on seismology (e.g., Wagner et al., 2005; Pesicek et al., 2012), volcanism (e.g. S. M. Kay & Abbruzzi, 1996; S. M. Kay & Mpodozis, 2002), gravity modeling (e.g. Sánchez et al., 2019) and electrical conductivity measurements (e.g. Burd et al., 2013, 2014). Scenarios for their formation have been explored with geodynamic modeling (e.g., Hu et al., 2016; Hu & Liu, 2016). In this study we focus on the Pampean flat subduction and Payenia steep subduction to the south, from 28°–38°S. Here, the Nazca slab is subducting beneath central Chile and western Argentina with a convergence rate of $\sim$6.7 $\mathrm{cm\,a^{-1}}$ in the N78°E direction (Kendrick et al., 2003). In the Pampean flat subduction zone, the Nazca slab propagates horizontally for 200-300 km beneath the southern Central Andes (Figure 1a). There is no consensus on a single mechanism for triggering flat subductions, but the following mechanisms have been proposed: (1) Increased buoyancy related to the presence of seamount chains or oceanic plateaus or younger age of the slab (e.g., Gans et al., 2011; Huangfu et al., 2016; Hu et al., 2016; S. Liu & Currie, 2016); (2) plate suction forces from a cold and/or over-thickened overriding plate with increased viscosity (e.g., Manea et al., 2012; Rodríguez-González et al., 2012); (3) increased movement of the overriding plate towards the trench and trench retreat (Schepers et al., 2017; Manea et al., 2017; S. Liu & Currie, 2016); (4) Over-pressure below the slab induced by mantle plumes (Boutelier & Cruden, 2008; Rodríguez-González et al., 2014). The Pampean flat subduction zone is believed to be associated with the subduction of the Juan Fernandez seamount ridge (JFR, Figure 1) (e.g. Gutscher et al., 2000; S. M. Kay & Mpodozis, 2002; Ramos et al., 2002). Plate reconstructions (Yáñez et al., 2001; Bello-González et al., 2018) indicate that the ridge has been moving southward along the western margin of South America. It was subducting beneath the Altiplano and Puna plateaus (21°-26°S) at $\sim$40-20 Ma, inducing inland migration of volcanism and a temporary lull between 20-12 Ma (Yáñez et al., 2001; S. M. Kay & Coira, 2009; Beck et al., 2015). The JFR arrived at the current position beneath the Sierras Pampeanas around 12 Ma (Figure 1) and the related flat subduction of the Nazca slab has triggered inland migration and spatial expansion of subduction-related volcanism (S. M. Kay & Mpodozis, 2002), uplift of the main Andes, thick-skinned deformation, crustal thickening and basement uplift over a broad zone in the overriding plate (Cristallini & Ramos, 2000; Ramos et al., 2002). The occurrence of adakitic magmatism has also been attributed to slab melting (Gutscher et al., 2000; Hu et al., 2016) or intrusion of the basaltic arc magmas (R. W. Kay & Kay, 2002).

In this study, we employ seismic full waveform inversion (FWI) to investigate the seismic structure in the upper mantle to understand the slab configuration changes and crustal melt distributions in response to the subduction of the JFR. For readability, we divide the whole study region into two domains (Figure 1a): the Pampean flat subduction zone in the north and the Payenia steep subduction zone in the south. The latter used to be a flat subduction zone from 15 Ma to 5 Ma but the slab has re-steepened since 4-5 Ma (S. M. Kay & Mpodozis, 2002; Ramos & Folguera, 2009).

2 Data and Method

Following the same workflow as Gao et al. (2021), we collected 139 earthquakes from the Global Centroid-Moment-Tensor (GCMT) catalog (Ekström et al., 2012), which were recorded by 19 seismic networks (Figure 1 and Figure S1) operating between 1996 to 2019 and magnitudes between M_W 5.0 to 7.0. Detailed network information and ray-path coverage are presented in the supplementary material (Figures S1–S2 and Table S1). Our seismic velocity model is the result of the multi-scale FWI based on the adjoint methodology (e.g., Fichtner et al., 2010; Tape et al., 2010), starting from the 3D seismic velocity model *S20RTS* (Ritsema et al., 2004). Solutions of the visco-elastic wave equation in a radially anisotropic Earth model are obtained from *Salvus* (Afanasiev et al., 2019). More information about the inversion workflow is provided in the supplementary material (Text S1).

In order to analyse the resolution of the inversion and trade-offs between the parameters, we calculated the Hessian-vector product Hδm as point-spread function to assess possible smearing and distortion (Fichtner & Trampert, 2011; Tao et al., 2018). We find that the isotropic V_S and V_P models are robustly determined in the resolved region with a spatial resolution of 30-40 km in the upper mantle and 20-25 km in the crust horizontally and vertically. Detailed resolution tests are described in Text S2 and Figure S18-S24.

3 Results and discussion

After 53 iterations of FWI, the crust and upper mantle structure beneath central Chile and western Argentina has been clearly imaged. We display the isotropic V_S model with some key depth and cross-sections. Further images and the isotropic V_P model are shown in the supplementary material (Figures S5–S16).

3.1 Multi-stage crustal partial melting and mantle wedge evolution

In contrast to the vigorous partial melting represented by strong low-velocity middle-crust beneath the Altiplano-Puna Volcanic Complex and volcanic arc for the northern Chile steep subduction zone (Yuan et al., 2000; Ward et al., 2014; Gao et al., 2021), the middle crust in the Pampean flat subduction zone (28°–33° S) exhibits only moderately low to normal velocities along the volcanic arc (Figure 2a).

Low-velocity anomaly C1 (Figure 2a and S17) is located beneath the Frontal Cordillera (FC) and has been reported by several earlier studies (e.g., Ward et al., 2013, 2017; Gao et al., 2021). C1 marks the waning partial melting beneath the Incapillo Caldera and Dome Complex (ICDC, Figure 1a), which is the southernmost ignimbritic caldera of the Central Andes during the Pleistocene (Goss et al., 2009, 2011). Meanwhile, weak and isolated low-velocity anomalies (C2 and C3, Figure 2a) beneath the Sierras Pampeanas (SP) are accompanied by middle to late Miocene adakitic volcanoes including the Famatina Mogotes Group (FMG, S. M. Kay & Mpodozis, 2002) and Gualcamayo Igneous Complex (GIC, D´Annunzio, Rubinstein, & Rabbia, 2018), indicating a slab melting origin or basaltic arc magma source (S. M. Kay & Abbruzzi, 1996; R. W. Kay & Kay, 2002; Gutscher et al., 2000; Hu & Liu, 2016).

A striking low-velocity anomaly C5 (Figure 2b and Profile (a) in Figure 3) at approximate Moho depth (60 km) extends from the Frontal Cordillera to the Sierras Pampeanas (SP), forming a thin layer above the Pampean flat slab. As the mantle wedge must have been thinned to a sliver or completely closed during the flattening of the Nazca slab (Gutscher et al., 2000; Manea et al., 2017), this low-velocity anomaly could be attributed to the combined effect of a fossil 'MASH' zone (melting-assimilation-storage-homogenization) and modern fluids released from the current flat slab (Hildreth & Moorbath, 1988). Dehydration of the flat slab has the potential to significantly modify the overriding lithosphere above it for a long distance from the trench (Z. Li, 2020). In Figure 3a-c, the continental mantle lithosphere south of 28°S appears to be thinned considerably or even displaced (Axen et al., 2018; Gutscher, 2018).

In contrast, south of 33°S, C4 may mark the restoration of partial melt accumulation in the middle crust during the re-steepening process of the Nazca slab beneath the Payenia (Marot et al., 2014; Ramos & Folguera, 2009). The late Miocene volcanic activity in the back-arc and Pleistocene-Holocene volcanic activity in the frontal arc (including large-scale Payenia Volcanic Province, Figure 1a) indicate a trench-ward migration of the volcanism.

Following the re-steepening of the slab since 4-5 Ma, the mantle wedge has re-opened, leading to the re-injection of hot asthenosphere and renewed melt formation in the wedge induced by slab-derived fluids dehydration, in turn inducing trench-ward migration of the volcanism (Gutscher et al., 2000; S. M. Kay & Mpodozis, 2002; Ramos & Folguera, 2009, 2011; Marot et al., 2014). The re-opened mantle wedge is clearly imaged in our model as low-velocity anomaly M3 and represents the present situation after the slab re-steepening (Figure 2c and profile (d) and (e) in Figure 3).

3.2 Slab thinning and tearing along the Juan Fernandez Ridge

In the central part of the Pampean flat slab, two low-velocity anomalies (M1 and M2) span a slab window along the inland projection of the JFR (Figure 2c and Profile (b) in Figure 3) and are surrounded by two high-velocity limbs of the flat slab (H2). Though many prior works detected the Pampean flat slab with strong heterogeneities, most of seismological studies focused on the seismic structure south of 29°S (e.g., Wagner et al., 2005; Porter et al., 2012; Marot et al., 2014; Linkimer et al., 2020), leaving an observational gap from 27°–29°S. In this study, events and stations north of 27°S are included in the inversion, allowing us to resolve M1 and M2.

The inland projection of the JFR is not well constrained from previous plate reconstruction studies (Yáñez et al., 2001; Bello-González et al., 2018) due to its relatively long subduction and migration history (12 Ma) beneath the Pampean area. Hence, the extent of the region affected by the JFR is not known precisely, nor are details of the seismic structure associated with the JFR (Gutscher et al., 2000; Wagner et al., 2005; Gans et al., 2011; Marot et al., 2014; Haddon & Porter, 2018). Following S. M. Kay and Mpodozis (2002), we assume the uncertainty width of the influence zone of the JFR within the oceanic lithosphere is 200 km, which also takes into account the region of underplating and possible hydration of the oceanic lithosphere (Kopp et al., 2004), which extends beyond the seamount chain itself. Thus, the low-velocity anomalies M1 and M2 are located within the JFR influence range. Similar to predictions from numerical modelling (Hu & Liu, 2016), the slab thinning and tearing zone develops within the central part of the current flat slab. In Hu & Liu's model, slab thinning and tearing initiates from the inboard tip of the flat slab before re-steepening downdip and propagates trench-wards, parallel to the track of the JFR and consistent our direct observation. In addition to the enhanced buoyancy of the JFR, its hydration state and inherited normal faults (Kopp et al., 2004) might have caused zones of weakness along which the thinning and tearing could progress.

Conspicuously, the slab tearing zone (M1 and M2) is characterized by the absence of intra-slab seismicity, in contrast to the slab limbs to the north and south (Fig. 2c). The focal mechanisms show a clear asymmetric pattern across the JFR track: the north branch of H2 is characterized by predominantly NE-SW oriented T axes, which are subparallel to the track of the JFR, whereas the T axes for events in the southern branch of H2 are oriented mainly NW-SE, sub-normal to the JFR trend, implying a $\sim 90°$ rotation of T axes across the aseismic zone (Figure 2c) at 120-160 km at depth. The northeast extension in the northern slab limb parallel to the JFR is superimposed on dominant slab pull (downdip extension), which is also reflected in the velocity field (Hu & Liu, 2016) and azimuthal anisotropy (Hu et al., 2017; Lynner et al., 2017). The south branch is coincident with the track of the JFR and attributed to the reactivation of the preexisting normal faults, causing vigorous intra-slab seismicity (Ranero et al., 2005; Anderson et al., 2007; Gans et al., 2011; Ammirati et al., 2015; Wagner et al., 2020).

Near the slab tearing zone, Heit et al. (2008) detected a strong oceanic LAB signal west of 69°W that suddenly disappears and even changes polarity further east (Profile (c) in Figure 3). Recent magnetic and gravity modeling work (Sánchez et al., 2019) also inferred hot asthenospheric flow beneath the flat slab and local slab thinning. These observations further validate our interpretation of M1 and M2 as evidence for thinning and tearing of the slab (Figure 4). M1 and M2 are also accompanied by weak crustal low-velocity anomalies C3 and C2 below the late Miocene adakitic volcanism including the GIC (D´Annunzio et al., 2018) and FMG (S. M. Kay & Mpodozis, 2002), respectively (Figure 2a), confirming enhanced slab melting (S. M. Kay & Mpodozis, 2002; Gutscher et al., 2000; Hu & Liu, 2016) near the tearing zone (Figure 4a).

The Pampean flat slab, after having developed in the Middle to Late Miocene, suffered from numerous instabilities, such as internal stresses induced by the increased buoyancy of the JFR relative to its two flanks, changes in hydration state, reactivation of inherited normal faults, and basal heating by asthenosphere flow (Rodríguez-González et al., 2014). These factors have induced weakening, thinning and finally tearing of the oceanic slab, followed by melting of the oceanic crust as predicted by the geodynamic model (Hu & Liu, 2016). The basalt input from the melted oceanic crust leads to the adakitic volcanism (Gutscher et al., 2000) during the late Miocene (Figure 4a).

3.3 Slab break-off: transition from steep to flat subduction?

A prominent high-velocity anomaly (H3) is found just below the flat Nazca slab (H2), extending from 28° S to 30° S (Figure 2d). At depth, H3 is dipping steeply to the east from 200 km down to 350 km depth (Profile (a), Figure 3). This anomaly was also visible in previous global or teleseismic tomography studies, but was so far not interpreted (e.g. C. Li et al., 2008; Portner et al., 2020; Mohammadzaheri et al., 2021). Recent S-wave teleseismic work (Rodríguez et al., 2021) captured a similar but larger-scale high-velocity anomaly extending from 200 km down to the lower mantle and attributed it to a part of relic Phoenix/Aluk plate, which was completely subducted by the late Cretaceous (Horton, 2018; Gianni et al., 2018). However, the resolution of the aforementioned models is limited in the upper mantle due to vertical smearing. We prefer to relate this anomaly to the more recent Nazca plate subduction as it seems unlikely that a part of the Phoenix slab could remain in the upper mantle for more than 100 million years and has not sunk into the lower mantle or thermally equilibrated with the surrounding mantle (Ramos & Folguera, 2009; Bello-González et al., 2018; Chen et al., 2019). Thus, we propose this anomaly to be a fossil fragment of the Nazca slab that was subducting steeply prior to the onset of flattening, indicating break-off from the leading edge of the current Nazca slab (S. Liu & Currie, 2016). Slab break-off during the slab flattening process is common in geodynamic models (e.g. Haschke et al., 2002; S. Liu & Currie, 2016; X. Liu & Currie, 2019; Dai et al., 2020). The conditions for slab break-off during the slab flattening process include fast trenchward migration of the overriding plate (high convergence rate) and a strong buoyancy contrast between either an oceanic plateau or aseismic ridge crust (here the JFR) and the normal thickness oceanic crust of an old slab (Haschke et al., 2002; Z. Li et al., 2011; S. Liu & Currie, 2016; X. Liu & Currie, 2019). The removal of the leading dense portion would allow the positive buoyancy of the trailing edge to quickly flatten out the slab (Figure 4b). In many global tomography models, the Nazca slab extends to much shallower depth in the south than the north, where it is visible down to 1000 km depth (C. Li et al., 2008; Obayashi et al., 2013). Several teleseismic tomography models (Portner et al., 2017, 2020; Rodríguez et al., 2021) for South America seem to indicate a slab hole at 200-300 km depth around 32°S in the re-steepened portion within the upper mantle. Thus the relic slab break-off or detachment from the head of the young and buoyant Nazca slab seems a viable option.

Taking account of the initial time of the transition from the steep to the flat subduction around 12 Ma coeval with the subduction of the JFR (Yáñez et al., 2001; S. M. Kay & Mpodozis, 2002; Ramos & Folguera, 2009), this would also be the time for the high density portion ahead of the JFR to break off from the leading edge of the young Nazca slab (Figure 4b). Furthermore, partial eclogitization of the oceanic crust before the onset of the flat subduction may play an important role in controlling the breaking-off time (X. Liu & Currie, 2019) and sinking depth in the upper mantle. Thus, the tail of the broken portion would sink slowly in the upper mantle due to its relatively young age, while the head would have already sunk into the mantle transition zone or deeper, below the resolution limit of our model. After break-off, the young and buoyant Nazca slab with the JFR could lift to extend horizontally eastwards for nearly 300 km before re-steepening with a steep angle to a relatively shallower depth compared to the dip subduction zone north of 28° S (Figure 4b).

3.4 Subslab asthenospheric flow induced by sudden re-steepening of the Nazca slab beneath the Payenia?

Another striking feature in our model is the low-velocity anomaly M4 extending from 32°–36°S below the steep Nazca slab in Payenia subduction zone and from slab depths to 250–300 km depth (Figures 2c and 3, Profile. (e)-(h)). This low-velocity anomaly has also been observed by some earlier tomography studies (Feng et al., 2007; Portner et al., 2017, 2020; Celli et al., 2020; Rodríguez et al., 2021). Portner et al. (2017) attributed it to the asthenosphere entrainment by the JFR with the subducting Nazca slab due to the coupling between the asthenosphere and overlying oceanic lithosphere (L. Liu & Zhou, 2015). However, due to its large size and location, it may more likely be caused by hot asthenospheric flow induced by the sudden re-steepening of the Nazca slab and trench retreat (Ramos & Folguera, 2009; Lin, 2014; Hu et al., 2017; Mohammadzaheri et al., 2021) since 4 Ma beneath the Payenia subduction zone (Figure 4a).

4 Conclusions

Through multi-scale full seismic waveform inversion, we identify low velocity zones within the Pampean flat slab parallel to the inland projection of the Juan Fernandez Ridge, which we interpret as a tearing zone within the flat slab. It may be induced by the buoyancy contrast between the Pampean flat slab with Juan Fernandez Ridge attached and its surrounding steep slab portions to the north and south. Meanwhile, the buoyancy contrast between the young Nazca slab and the preceding steep Nazca slab appears to have triggered the slab break-off from the leading edge of current Nazca slab. The resulting buoyancy increase could possibly sustain the long-distance flat subduction. Flat subduction also expelled the mantle wedge and shut off partial melting, resulting in much reduced volcanic activity and presence of partial melt in the crust. Re-steepening of the Nazca slab beneath the Payenia subduction zone seems to have significantly perturbed the sub-slab asthenospheric flow and introduced large-scale mantle flow, as visible in large low-velocity zone both above and below the slab. Re-opening of the mantle wedge and injection of the asthenosphere induced by the re-steepening of the Nazca slab may have caused the re-accumulation of partial melts within the middle crust and volcanic arc trench-ward migration and reactivation.

Acknowledgments

We gratefully acknowledge fruitful discussions with Lara S. Wagner, Jiashun Hu, Lijun Liu, Xiaowen Liu, Guohui Li, Wei Li, Tuo Zhang, Youqiang Yu. This work was supported by the Swiss National Supercomputing Center (CSCS) in the form of computing time grants s868 and s1040. Yajian Gao is sponsored by Freie Universität Berlin - China Scholarship Council Programm. Dirk-Philip van Herwaarden and Solvi Thrastarson were supported by the European Research Council (ERC) under the EU's Horizon 2020 programme (grant No. 714069).

Data Availability

Waveform data and station meta data were downloaded using the ObsPy (Krischer et al., 2015) module through the International Federation of Digital Seismograph Networks (FDSN) webservices from GEOFON Data Management Center (`https://geofon.gfz-potsdam.de/waveform/archive/`) and Incorporated Research Institutions for Seismology Data Management Center (`IRIS-DMC,http://www.iris.edu/ds/nodes/dmc/`). Raw data of the temporary and permanent networks used in this study with FDSN codes including C (`https://www.fdsn.org/networks/detail/C/`); C1 (`https://doi.org/10.7914/SN/C1`); CX (`https://doi.org/10.14470/PK615318`); GT(`https://doi.org/10.7914/SN/GT`); IU (`https://doi.org/10.7914/SN/IU`); WA (`https://www.fdsn.org/networks/detail/WA/`); 2B (`https://doi.org/10.14470/7O092361`); 3A (`https://www.fdsn.org/networks/detail/3A_2010/`); 3H(`https://doi.org/10.14470/8U7569253520`); G (`https://doi.org/10.18715/GEOSCOPE.G`); X6(`https://doi.org/10.7914/SN/X6_2007`); XH(`https://doi.org/10.7914/SN/XH_2008`); XS(`https://doi.org/10.15778/RESIF.XS2010`); XY(`https://doi.org/10.7914/SN/XY_2010`); YC(`https://doi.org/10.7914/SN/YC_2000`); YM(`https://doi.org/10.7914/SN/YM_2010`); ZA(`https://doi.org/10.14470/MN7557778612`); ZB(`https://doi.org/10.14470/MO6442843258`); ZE(`https://www.fdsn.org/networks/detail/ZE_2010/`);

ZL(`https://doi.org/10.7914/SN/ZL_2007`); ZP(`https://www.fdsn.org/networks/detail/ZP_1999/`); ZQ(`https://www.fdsn.org/networks/detail/ZQ_2004/`); ZW(`https://doi.org/10.14470/MJ7559637482`);

References

Afanasiev, M., Boehm, C., Van Driel, M., Krischer, L., Rietmann, M., May, D. A., ... Fichtner, A. (2019). Modular and flexible spectral-element waveform modelling in two and three dimensions. *Geophysical Journal International*, *216*(3), 1675–1692. doi: https://doi.org/10.1093/gji/ggy469

Amante, C., & Eakins, B. W. (2009). *ETOPO1 Global Relief Model converted to PanMap layer format.* PANGAEA. doi: https://doi.org/10.1594/PANGAEA.769615

Ammirati, J. B., Alvarado, P., & Beck, S. L. (2015). A lithospheric velocity model for the flat slab region of Argentina from joint inversion of Rayleigh wave phase velocity dispersion and teleseismic receiver functions. *Geophysical Journal International*, *202*(1), 224–241. doi: https://doi.org/10.1093/gji/ggv140

Anderson, M., Alvarado, P., Zandt, G., & Beck, S. L. (2007). Geometry and brittle deformation of the subducting Nazca Plate, Central Chile and Argentina. *Geophysical Journal International*, *171*(1), 419–434. doi: https://doi.org/10.1111/j.1365-246X.2007.03483.x

Axen, G. J., van Wijk, J. W., & Currie, C. A. (2018). Basal continental mantle lithosphere displaced by flat-slab subduction. *Nature Geoscience*, *11*(12), 961–964. doi: https://doi.org/10.1038/s41561-018-0263-9

Beck, S. L., Zandt, G., Ward, K. M., & Scire, A. (2015). Multiple styles and scales of lithospheric foundering beneath the Puna Plateau, central Andes. In *Geodynamics of a Cordilleran Orogenic System: The Central Andes of Argentina and Northern Chile.* Geological Society of America. doi: https://doi.org/10.1130/2015.1212(03)

Bello-González, J. P., Contreras-Reyes, E., & Arriagada, C. (2018). Predicted path for hotspot tracks off South America since Paleocene times: Tectonic implications of ridge-trench collision along the Andean margin. *Gondwana Research*, *64*, 216–234. doi: https://doi.org/10.1016/j.gr.2018.07.008

Boutelier, D. A., & Cruden, A. R. (2008). Impact of regional mantle flow on subducting plate geometry and interplate stress: insights from physical modelling. *Geophysical Journal International*, *174*(2), 719–732. doi: https://doi.org/10.1111/j.1365-246X.2008.03826.x

Burd, A. I., Booker, J. R., Mackie, R., Favetto, A., & Pomposiello, M. C. (2014). Three-dimensional electrical conductivity in the mantle beneath the Payún Matrú Volcanic Field in the Andean backarc of Argentina near 36.5 S: Evidence for decapitation of a mantle plume by resurgent upper mantle shear during slab steepening. *Geophysical Journal International*, *198*(2), 812–827. doi: https://doi.org/10.1093/gji/ggu145

Burd, A. I., Booker, J. R., Mackie, R., Pomposiello, M. C., & Favetto, A. (2013). Electrical conductivity of the pampean shallow subduction region of argentina near 33 s: Evidence for a slab window. *Geochemistry, Geophysics, Geosystems*, *14*(8), 3192–3209. doi: https://doi.org/10.1002/ggge.20213

Celli, N. L., Lebedev, S., Schaeffer, A. J., Ravenna, M., & Gaina, C. (2020). The upper mantle beneath the South Atlantic Ocean, South America and Africa from waveform tomography with massive data sets. *Geophysical Journal International*, *221*(1), 178-204. doi: https://doi.org/10.1093/gji/ggz574

Chen, Y. W., Wu, J., & Suppe, J. (2019). Southward propagation of Nazca subduction along the Andes. *Nature*, *565*(7740), 441–447. doi: https://doi.org/10.1038/s41586-018-0860-1

Cristallini, E. O., & Ramos, V. A. (2000). Thick-skinned and thin-skinned thrusting in the La Ramada fold and thrust belt: crustal evolution of the High Andes of San Juan, Argentina (32 SL). *Tectonophysics*, *317*(3-4), 205–235. doi: https://doi.org/10.1016/S0040-1951(99)00276-0

Dai, L., Wang, L., Lou, D., Li, Z.-H., Dong, H., Ma, F., … Yu, S. (2020). Slab rollback versus delamination: Contrasting fates of flat-slab subduction and implications for South China evolution in the Mesozoic. *Journal of Geophysical Research: Solid Earth*, *125*(4), e2019JB019164. doi: https://doi.org/10.1029/2019JB019164

D´Annunzio, M. C., Rubinstein, N., & Rabbia, O. (2018). Petrogenesis of the Gualcamayo Igneous Complex: Regional implications of Miocene magmatism in the Precordillera over the Pampean flat-slab segment, Argentina. *Journal of South American Earth Sciences*, *88*, 16-28. doi: https://doi.org/10.1016/j.jsames.2018.06.012

Ekström, G., Nettles, M., & Dziewoński, A. (2012). The global CMT project 2004–2010: Centroid-moment tensors for 13,017 earthquakes. *Physics of the Earth and Planetary Interiors*, *200-201*, 1 - 9. doi: https://doi.org/10.1016/j.pepi.2012.04.002

Engdahl, E. R., Di Giacomo, D., Sakarya, B., Gkarlaouni, C. G., Harris, J., & Storchak, D. A. (2020). ISC-EHB 1964–2016, an Improved Data Set for Studies of Earth Structure and Global Seismicity. *Earth and Space Science*, *7*(1), e2019EA000897. doi: https://doi.org/10.1029/2019EA000897

Feng, M., Van der Lee, S., & Assumpção, M. (2007). Upper mantle structure of South America from joint inversion of waveforms and fundamental mode group velocities of Rayleigh waves. *Journal of Geophysical Research: Solid Earth*, *112*(B4). doi: https://doi.org/10.1029/2006JB004449

Fichtner, A., Kennett, B. L., Igel, H., & Bunge, H.-P. (2010). Full waveform tomography for radially anisotropic structure: new insights into present and past states of the Australasian upper mantle. *Earth and Planetary Science Letters*, *290*(3-4), 270–280. doi: https://doi.org/10.1016/j.epsl.2009.12.003

Fichtner, A., & Trampert, J. (2011). Resolution analysis in full waveform inversion. *Geophysical Journal International*, *187*(3), 1604–1624. doi: https://doi.org/10.1111/j.1365-246X.2011.05218.x

Gans, C. R., Beck, S. L., Zandt, G., Gilbert, H., Alvarado, P., Anderson, M., & Linkimer, L. (2011). Continental and oceanic crustal structure of the Pampean flat slab region, western Argentina, using receiver function analysis: New high-resolution results. *Geophysical Journal International*, *186*(1), 45–58. doi: https://doi.org/10.1111/j.1365-246X.2011.05023.x

Gao, Y., Tilmann, F., van Herwaarden, D.-P., Thrastarson, S., Fichtner, A., Heit, B., … Schurr, B. (2021). Full Waveform Inversion beneath the Central Andes: Insight into the dehydration of the Nazca slab and delamination of the back-arc lithosphere. *Journal of Geophysical Research: Solid Earth*, *126*(7), e2021JB021984. doi: https://doi.org/10.1029/2021JB021984

Gianni, G., Pesce, A., & Soler, S. (2018). Transient plate contraction between two simultaneous slab windows: Insights from Paleogene tectonics of the Patagonian Andes. *Journal of Geodynamics*, *121*, 64-75. doi: https://doi.org/10.1016/j.jog.2018.07.008

Goss, A. R., Kay, S., Mpodozis, C., & Singer, B. (2009). The Incapillo Caldera and Dome Complex (28 S, central Andes): A stranded magma chamber over a dying arc. *Journal of volcanology and geothermal research*, *184*(3-4), 389–404. doi: https://doi.org/10.1016/j.jvolgeores.2009.05.005

Goss, A. R., Kay, S. M., & Mpodozis, C. (2011). The geochemistry of a dying continental arc: the Incapillo Caldera and Dome Complex of the southernmost Central Andean Volcanic Zone (˜28 S). *Contributions to Mineralogy and Petrology*, *161*(1), 101–128. doi: https://doi.org/10.1007/s00410-010-0523-1

Gutscher, M.-A. (2018). Scraped by flat-slab subduction. *Nature Geoscience*, *11*(12), 890–891. doi: https://doi.org/10.1038/s41561-018-0270-x

Gutscher, M.-A., Maury, R., Eissen, J.-P., & Bourdon, E. (2000). Can slab melting be caused by flat subduction? *Geology*, *28*(6), 535–538.

Haddon, A., & Porter, R. (2018). S-Wave Receiver Function Analysis of the Pampean Flat-Slab Region: Evidence for a Torn Slab. *Geochemistry, Geophysics, Geosystems*, *19*(10), 4021-4034. doi: https://doi.org/10.1029/2018GC007868

Haschke, M., Scheuber, E., Günther, A., & Reutter, K.-J. (2002). Evolutionary cycles during the Andean orogeny: repeated slab breakoff and flat subduction? *Terra nova*, *14*(1), 49–55. doi: https://doi.org/10.1046/j.1365-3121.2002.00387.x

Hayes, G. P., Moore, G. L., Portner, D. E., Hearne, M., Flamme, H., Furtney, M., & Smoczyk, G. M. (2018). Slab2, a comprehensive subduction zone geometry model. *Science*, *362*(6410), 58–61. doi: https://doi.org/10.1126/science.aat4723

Heit, B., Yuan, X., Bianchi, M., Sodoudi, F., & Kind, R. (2008). Crustal thickness estimation beneath the southern central Andes at 30°S and 36°S from S wave receiver function analysis. *Geophysical Journal International*, *174*(1), 249-254. doi: https://doi.org/10.1111/j.1365-246X.2008.03780.x

Hildreth, W., & Moorbath, S. (1988). Crustal contributions to arc magmatism in the Andes of central Chile. *Contributions to mineralogy and petrology*, *98*(4), 455–489. doi: https://doi.org/10.1007/BF00372365

Horton, B. K. (2018). Tectonic Regimes of the Central and Southern Andes: Responses to Variations in Plate Coupling During Subduction. *Tectonics*, *37*(2), 402–429. doi: https://doi.org/10.1002/2017TC004624

Hu, J., Faccenda, M., & Liu, L. (2017). Subduction-controlled mantle flow and seismic anisotropy in South America. *Earth and Planetary Science Letters*, *470*, 13–24. doi: https://doi.org/10.1016/j.epsl.2017.04.027

Hu, J., & Liu, L. (2016). Abnormal seismological and magmatic processes controlled by the tearing South American flat slabs. *Earth and Planetary Science Letters*, *450*, 40–51. doi: https://doi.org/10.1016/j.epsl.2016.06.019

Hu, J., Liu, L., Hermosillo, A., & Zhou, Q. (2016). Simulation of late Cenozoic South American flat-slab subduction using geodynamic models with data assimilation. *Earth and Planetary Science Letters*, 1–13. doi: https://doi.org/10.1016/j.epsl.2016.01.011

Huangfu, P., Wang, Y., Cawood, P. A., Li, Z.-H., Fan, W., & Gerya, T. V. (2016). Thermo-mechanical controls of flat subduction: Insights from numerical modeling. *Gondwana Research*, *40*, 170–183. doi: https://doi.org/10.1016/j.gr.2016.08.012

Kay, R. W., & Kay, S. M. (2002). Andean adakites: three ways to make them. *Acta Petrologica Sinica*, *18*(3), 303–311.

Kay, S. M., & Abbruzzi, J. (1996). Magmatic evidence for Neogene lithospheric evolution of the central Andean "flat-slab" between 30 S and 32 S. *Tectonophysics*, *259*(1-3), 15–28. doi: https://doi.org/10.1016/0040-1951(96)00032-7

Kay, S. M., & Coira, B. L. (2009). Shallowing and steepening subduction zones, continental lithospheric loss, magmatism, and crustal flow under the Central Andean Altiplano-Puna Plateau. *Backbone of the Americas: shallow subduction, plateau uplift, and ridge and terrane collision*, *204*, 229. doi: https://doi.org/10.1130/2009.1204(11)

Kay, S. M., & Mpodozis, C. (2002). Magmatism as a probe to the Neogene shallowing of the Nazca plate beneath the modern Chilean flat-slab. *Journal of South American Earth Sciences*, *15*(1), 39–57. doi: https://doi.org/10.1016/S0895-9811(02)00005-6

Kendrick, E., Bevis, M., Smalley Jr, R., Brooks, B., Vargas, R. B., Laurıa, E., & Fortes, L. P. S. (2003). The Nazca–South America Euler vector and its rate of change. *Journal of South American Earth Sciences*, *16*(2), 125-131. doi: https://doi.org/10.1016/S0895-9811(03)00028-2

Kopp, H., Flueh, E. R., Papenberg, C., & Klaeschen, D. (2004). Seismic investigations of the O'Higgins Seamount Group and Juan Fernández Ridge: Aseismic ridge emplacement and lithosphere hydration. *Tectonics*, *23*(2), 1–21. doi: https://doi.org/10.1029/2003TC001590

Krischer, L., Megies, T., Barsch, R., Beyreuther, M., Lecocq, T., Caudron, C., & Wassermann, J. (2015). ObsPy: a bridge for seismology into the scientific python ecosystem. *Computational Science & Discovery*, *8*(1), 014003. doi: https://doi.org/10.1088/1749-4699/8/1/014003

Li, C., Van Der Hilst, R. D., Engdahl, E. R., & Burdick, S. (2008). A new global model for P wave speed variations in Earth's mantle. *Geochemistry, Geophysics, Geosystems*, *9*(5). doi: https://doi.org/10.1029/2007GC001806

Li, Z. (2020). Flat subduction versus big mantle wedge: contrasting modes for deep hydration and overriding craton modification. *Journal of Geophysical Research: Solid Earth*, *125*(8). doi: https://doi.org/10.1029/2020JB020018

Li, Z., Xu, Z., & Gerya, T. (2011). Flat versus steep subduction: Contrasting modes for the formation and exhumation of high-to ultrahigh-pressure rocks in continental collision zones. *Earth and Planetary Science Letters*, *301*(1-2), 65–77. doi: https://doi.org/10.1016/j.epsl.2010.10.014

Lin, S. (2014). Three-dimensional mantle circulations and lateral slab deformation in the southern Chilean subduction zone. *Journal of Geophysical Research: Solid Earth*, *119*(4), 3879–3896. doi: https://doi.org/10.1002/2013JB010864

Linkimer, L., Beck, S., Zandt, G., Alvarado, P., Anderson, M., Gilbert, H., & Zhang, H.

(2020). Lithospheric structure of the Pampean flat slab region from double-difference tomography. *Journal of South American Earth Sciences*, *97*, 102417. doi: https://doi.org/10.1016/j.jsames.2019.102417

Liu, L., & Zhou, Q. (2015). Deep recycling of oceanic asthenosphere material during subduction. *Geophysical Research Letters*, *42*(7), 2204–2211. doi: https://doi.org/10.1002/2015GL063633

Liu, S., & Currie, C. A. (2016). Farallon plate dynamics prior to the Laramide orogeny: Numerical models of flat subduction. *Tectonophysics*, *666*, 33–47. doi: https://doi.org/10.1016/j.tecto.2015.10.010

Liu, X., & Currie, C. A. (2019). Influence of upper plate structure on flat-slab depth: Numerical modeling of subduction dynamics. *Journal of Geophysical Research: Solid Earth*, *124*(12), 13150–13167. doi: https://doi.org/10.1029/2019JB018653

Lynner, C., Anderson, M. L., Portner, D. E., Beck, S. L., & Gilbert, H. (2017). Mantle flow through a tear in the Nazca slab inferred from shear wave splitting. *Geophysical Research Letters*, *44*(13), 6735–6742. doi: https://doi.org/10.1002/2017GL074312

Manea, V. C., Manea, M., Ferrari, L., Orozco-Esquivel, T., Valenzuela, R., Husker, A., & Kostoglodov, V. (2017). A review of the geodynamic evolution of flat slab subduction in Mexico, Peru, and Chile. *Tectonophysics*, *695*, 27–52. doi: https://doi.org/10.1016/j.tecto.2016.11.037

Manea, V. C., Pérez-Gussinyé, M., & Manea, M. (2012). Chilean flat slab subduction controlled by overriding plate thickness and trench rollback. *Geology*, *40*(1), 35–38. doi: https://doi.org/10.1130/G32543.1

Marot, M., Monfret, T., Gerbault, M., Nolet, G., Ranalli, G., & Pardo, M. (2014). Flat versus normal subduction zones: A comparison based on 3-D regional traveltime tomography and petrological modelling of central Chile and western Argentina (29°-35°S). *Geophysical Journal International*, *199*(3), 1633–1654. doi: https://doi.org/10.1093/gji/ggu355

Mohammadzaheri, A., Sigloch, K., Hosseini, K., & Mihalynuk, M. G. (2021). Subducted Lithosphere Under South America From Multifrequency P Wave Tomography. *Journal of Geophysical Research: Solid Earth*, *126*(6), e2020JB020704. doi: https://doi.org/10.1029/2020JB020704

Obayashi, M., Yoshimitsu, J., Nolet, G., Fukao, Y., Shiobara, H., Sugioka, H., . . . Gao, Y. (2013). Finite frequency whole mantle P wave tomography: Improvement of subducted slab images. *Geophysical Research Letters*, *40*(21), 5652–5657.

Pesicek, J., Engdahl, E., Thurber, C., DeShon, H., & Lange, D. (2012). Mantle subducting slab structure in the region of the 2010 M 8.8 Maule earthquake (30–40 S), Chile. *Geophysical Journal International*, *191*(1), 317–324. doi: https://doi.org/10.1111/j.1365-246X.2012.05624.x

Piceda, C. R., Wenderoth, M. S., Dacal, M. L. G., Bott, J., Prezzi, C. B., & Strecker, M. R. (2020). Lithospheric density structure of the Southern Central Andes constrained by 3D data-integrative gravity modelling. *International Journal of Earth Sciences*, 1–27. doi: https://doi.org/10.1007/s00531-020-01962-1

Porter, R., Gilbert, H., Zandt, G., Beck, S., Warren, L., Calkins, J., . . . Anderson, M. (2012). Shear wave velocities in the Pampean flat-slab region from Rayleigh wave tomography: Implications for slab and upper mantle hydration. *Journal of Geophysical Research B: Solid Earth*, *117*(11), 1–21. doi: https://doi.org/10.1029/2012JB009350

Portner, D. E., Beck, S., Zandt, G., & Scire, A. (2017). The nature of subslab slow velocity anomalies beneath South America. *Geophysical Research Letters*, *44*(10), 4747–4755. doi: https://doi.org/10.1002/2017GL073106

Portner, D. E., Rodríguez, E. E., Beck, S. L., Zandt, G., Scire, A., Rocha, M. P., . . . Alvarado, P. (2020). Detailed Structure of the Subducted Nazca Slab into the Lower Mantle Derived From Continent-Scale Teleseismic P Wave Tomography. *Journal of Geophysical Research: Solid Earth*, *125*(5). doi: https://doi.org/10.1029/2019JB017884

Ramos, V. A., Cristallini, E. O., & Pérez, D. J. (2002). The Pampean flat-slab of the Central Andes. *Journal of South American earth sciences*, *15*(1), 59–78. doi: https://doi.org/10.1016/S0895-9811(02)00006-8

Ramos, V. A., & Folguera, A. (2009). Andean flat-slab subduction through time. *Geological Society, London, Special Publications*, *327*(1), 31–54. doi: https://doi.org/10.1144/SP327.3

Ramos, V. A., & Folguera, A. (2011). Payenia volcanic province in the Southern Andes: An appraisal of an exceptional Quaternary tectonic setting. *Journal of Volcanology and geothermal Research*, *201*(1-4), 53–64. doi: https://doi.org/10.1016/j.jvolgeores.2010.09.008

Ranero, C. R., Villaseñor, A., Phipps Morgan, J., & Weinrebe, W. (2005). Relationship between bend-faulting at trenches and intermediate-depth seismicity. *Geochemistry, Geophysics, Geosystems*, *6*(12). doi: http://dx.doi.org/10.1029/2005GC000997

Ritsema, J., van Heijst, H. J., & Woodhouse, J. H. (2004). Global transition zone tomography. *Journal of Geophysical Research: Solid Earth*, *109*(B2). doi: https://doi.org/10.1029/2003JB002610

Rivadeneyra-Vera, C., Bianchi, M., Assumpção, M., Cedraz, V., Julià, J., Rodríguez, M., … others (2019). An updated crustal thickness map of central South America based on receiver function measurements in the region of the Chaco, Pantanal, and Paraná Basins, southwestern Brazil. *Journal of Geophysical Research: Solid Earth*, *124*(8), 8491–8505. doi: https://doi.org/10.1029/2018JB016811

Rodríguez, E. E., Portner, D. E., Beck, S. L., Rocha, M. P., Bianchi, M. B., Assumpção, M., … Lynner, C. (2021). Mantle dynamics of the Andean Subduction Zone from continent-scale teleseismic S-wave tomography. *Geophysical Journal International*, *224*(3), 1553–1571. doi: https://doi.org/10.1093/gji/ggaa536

Rodríguez-González, J., Negredo, A. M., & Billen, M. I. (2012). The role of the overriding plate thermal state on slab dip variability and on the occurrence of flat subduction. *Geochemistry, Geophysics, Geosystems*, *13*(1). doi: https://doi.org/10.1029/2011GC003859

Rodríguez-González, J., Negredo, A. M., & Carminati, E. (2014). Slab–mantle flow interaction: influence on subduction dynamics and duration. *Terra Nova*, *26*(4), 265–272. doi: https://doi.org/10.1111/ter.12095

Sánchez, M. A., García, H. P., Acosta, G., Gianni, G. M., Gonzalez, M. A., Ariza, J. P., … Folguera, A. (2019). Thermal and lithospheric structure of the Chilean-Pampean flat-slab from gravity and magnetic data. In *Andean tectonics* (pp. 487–507). Elsevier. doi: https://doi.org/10.1016/B978-0-12-816009-1.00005-8

Schepers, G., Van Hinsbergen, D. J., Spakman, W., Kosters, M. E., Boschman, L. M., & McQuarrie, N. (2017). South-American plate advance and forced Andean trench retreat as drivers for transient flat subduction episodes. *Nature Communications*, *8*(0316), 1–9. doi: https://doi.org/10.1038/ncomms15249

Sippl, C., Moreno, M., & Benavente, R. (2020). Microseismicity appears to outline highly coupled regions on the Central Chile megathrust. *EarthArXiv*. doi: https://doi.org/10.31223/X56S3B

Tao, K., Grand, S. P., & Niu, F. (2018). Seismic Structure of the Upper Mantle Beneath Eastern Asia From Full Waveform Seismic Tomography. *Geochemistry, Geophysics, Geosystems*, *19*(8), 2732-2763. doi: https://doi.org/10.1029/2018GC007460

Tape, C., Liu, Q., Maggi, A., & Tromp, J. (2010). Seismic tomography of the southern California crust based on spectral-element and adjoint methods. *Geophysical Journal International*, *180*(1), 433–462. doi: https://doi.org/10.1111/j.1365-246X.2009.04429.x

Tassara, A., Götze, H.-J., Schmidt, S., & Hackney, R. (2006). Three-dimensional density model of the Nazca plate and the Andean continental margin. *Journal of Geophysical Research: Solid Earth*, *111*(B9). doi: https://doi.org/10.1029/2005JB003976

Wagner, L. S., Beck, S., & Zandt, G. (2005). Upper mantle structure in the south central chilean subduction zone (30 to 36 s). *Journal of Geophysical Research: Solid Earth*, *110*(B1). doi: https://doi.org/10.1029/2004JB003238

Wagner, L. S., Caddick, M. J., Kumar, A., Beck, S. L., & Long, M. D. (2020). Effects of Oceanic Crustal Thickness on Intermediate Depth Seismicity. *Frontiers in Earth Science*, *8*(July). doi: https://doi.org/10.3389/feart.2020.00244

Ward, K. M., Delph, J. R., Zandt, G., Beck, S. L., & Ducea, M. N. (2017). Magmatic evolution of a Cordilleran flare-up and its role in the creation of silicic crust. *Scientific Reports*, *7*(1), 1–8. doi: https://doi.org/10.1038/s41598-017-09015-5

Ward, K. M., Porter, R. C., Zandt, G., Beck, S. L., Wagner, L. S., Minaya, E., & Tavera, H. (2013). Ambient noise tomography across the Central Andes. *Geophysical Journal International*, *194*(3), 1559-1573. doi: https://doi.org/10.1093/gji/ggt166

Ward, K. M., Zandt, G., Beck, S. L., Christensen, D. H., & McFarlin, H. (2014). Seismic imaging of the magmatic underpinnings beneath the altiplano-puna volcanic complex from the joint inversion of surface wave dispersion and receiver functions. *Earth and Planetary Science Letters*, *404*, 43 - 53. doi: https://doi.org/10.1016/j.epsl.2014.07.022

Yáñez, G. A., Ranero, C. R., Von Huene, R., & Díaz, J. (2001). Magnetic anomaly interpretation across the southern central Andes (32°-34°S): The role of the Juan Fernández Ridge in the late Tertiary evolution of the margin. *Journal of Geophysical Research: Solid Earth*, *106*(B4), 6325–6345. doi: https://doi.org/10.1029/2000jb900337

Yuan, X., Sobolev, S. V., Kind, R., Oncken, O., Bock, G., Asch, G., … Comte, D. (2000). Subduction and collision processes in the Central Andes constrained by converted seismic phases. *Nature*, *408*(6815), 958-961. doi: 10.1038/35050073

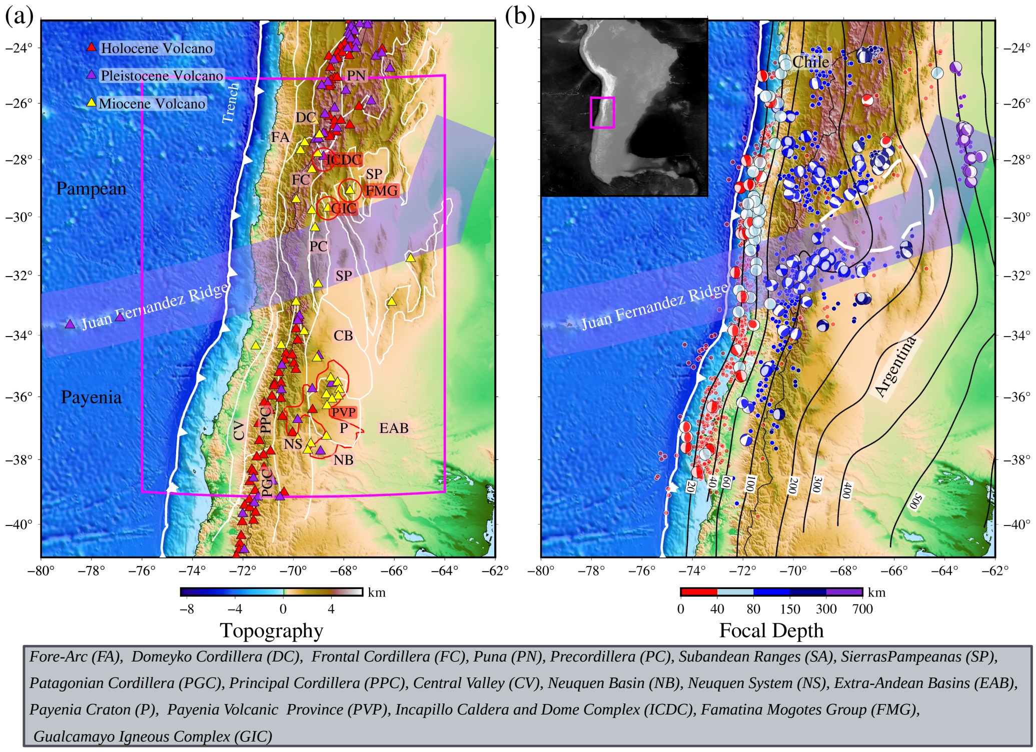

Figure 1. (a) Map of major morphotectonic provinces (modified from Tassara et al. (2006); Piceda et al. (2020)). Red solid line denotes the Payenia Volcanic Province (Ramos & Folguera, 2011). White saw-tooth line denotes the trench. (b) Map showing focal mechanisms of the earthquakes used for FWI. Color-coded circles represent the seismicity (magnitude > Mw 4.0) retrieved from the ISC-EHB catalog (Engdahl et al., 2020). Black solid lines denote the Nazca slab contours from Slab 2.0 (Hayes et al., 2018). Inset map marks the position of our study region. Topography data is retrieved from ETOPO1 Global Relief Model (Amante & Eakins, 2009).

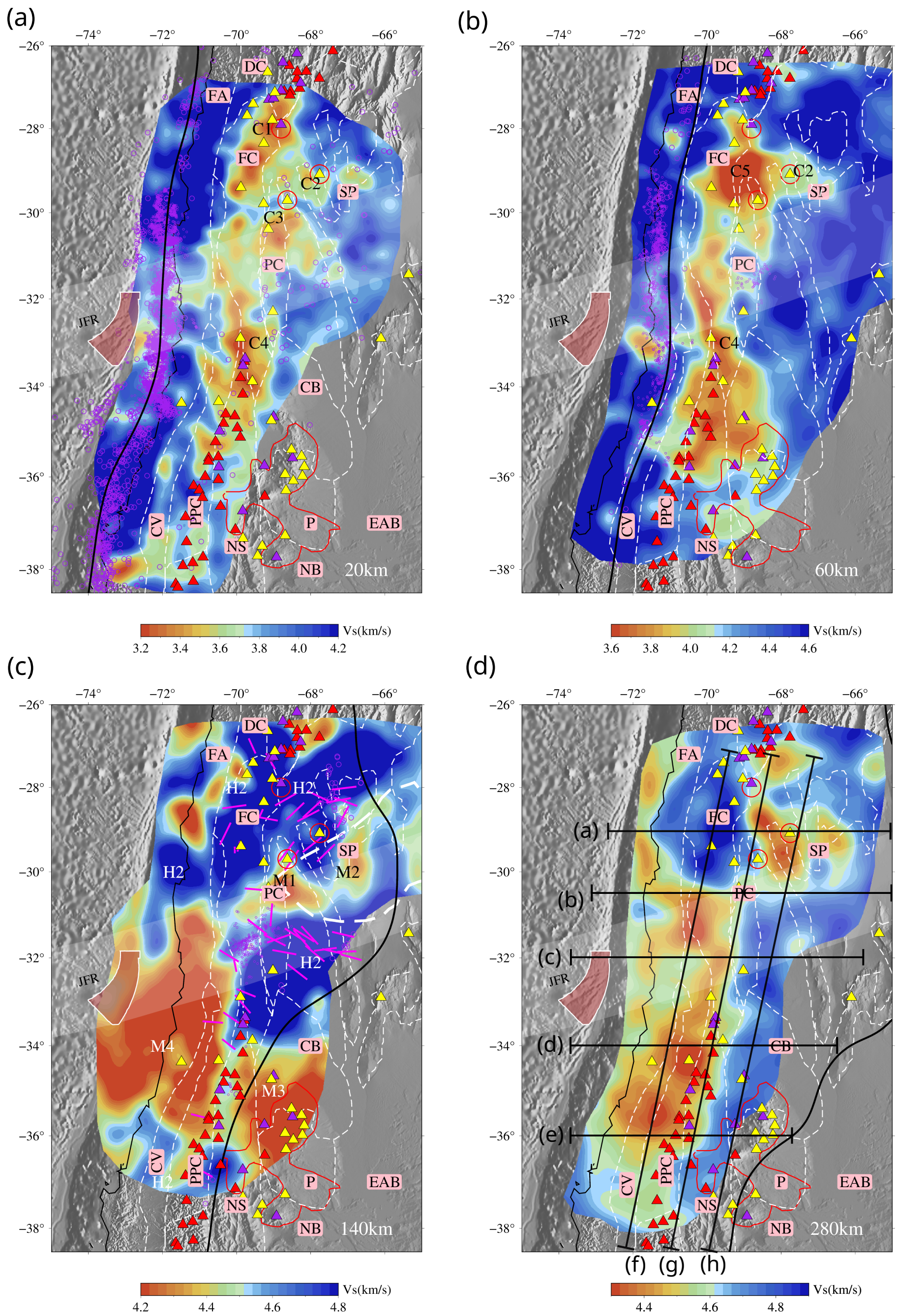

Figure 2. Horizontal slices for isotropic V_S at 20 km (a), 60 km (b), 140 km (c), and 280 km (d). In (c) T (tension) axes from GCMT focal mechanism solutions (Ekström et al., 2012) for earthquakes between 120 and 150 km depth with magnitude M_W >5.0 are indicated by magenta bars. The large and small magenta circles are seismicity from ISC-EHB catalog and the relocated catalog from Sippl et al. (2020), respectively, and within 10 km of the nominal depth of the slice. The pink shaded area off-shore indicates the position of the weakened oceanic lithosphere detected by Kopp et al. (2004) along the JFR. Solid black lines denote the top of the slab according to Slab 2.0 (Hayes et al., 2018) at the depth of the slice. Black straight lines in (d) denote the positions of the cross-sections in Figure 3.

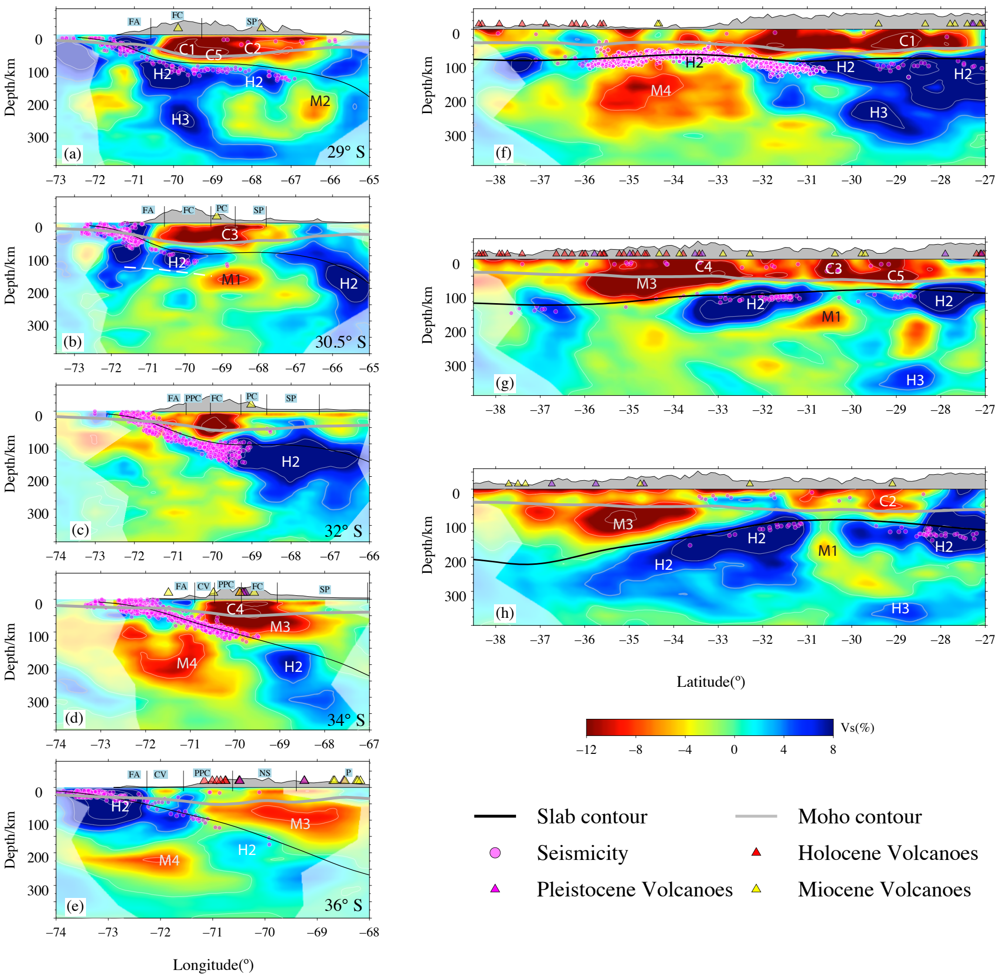

Figure 3. Cross-sections of isotropic V_S perturbation relative to the reference 1D V_S defined in Figure S3. (see Figure 2d for profile locations). Thick solid black lines denote the continental Moho (Rivadeneyra-Vera et al., 2019) and thin solid black lines denote the slab contour from Slab 2.0 (Hayes et al., 2018). The thick white dashed line in b denotes the oceanic LAB from receiver function (Heit et al., 2008). Magenta dots in b-d denote the seismicity relocated by Sippl et al. (2020) and in other profiles are retrieved from ISC-EHB catalog.

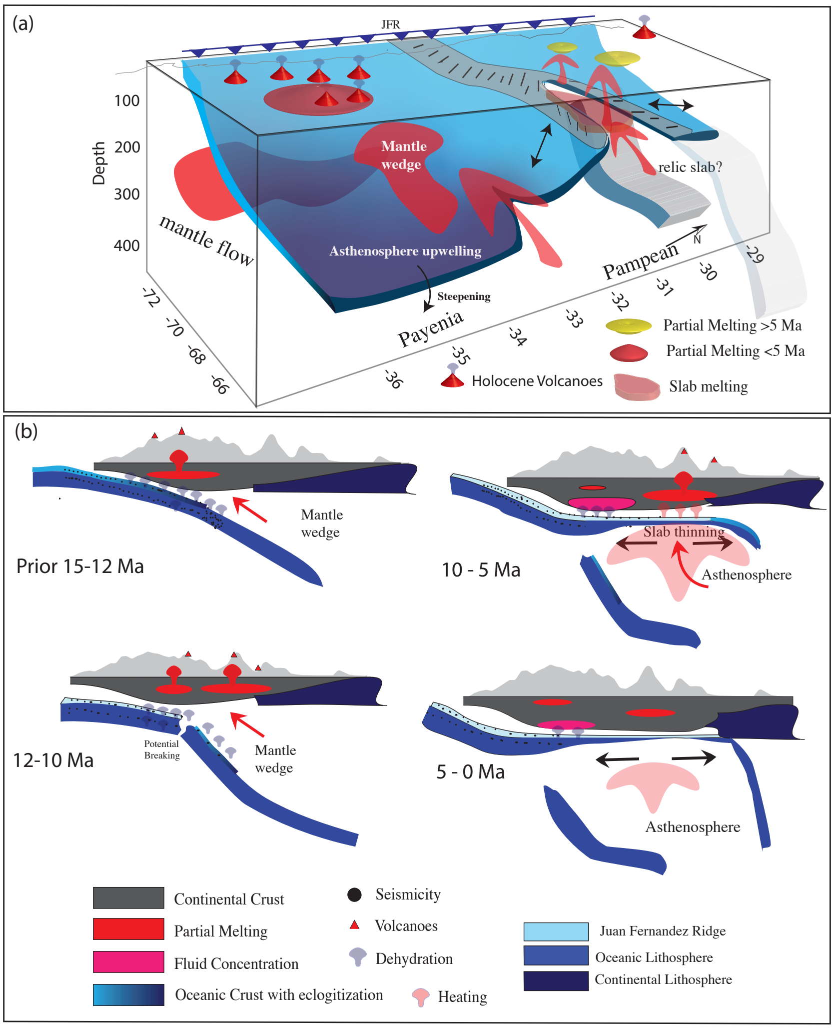

Figure 4. (a) Schematic representation of the current Nazca slab configuration west of 66°W. Gray zone with short bars indicates the inland projection of the Juan Fernandez Ridge. South of 33°S the Nazca plate subducts steeply in the Payenia segment. (b) Proposed sequence of the steep to flat slab subduction evolution along 29°S since 12 Ma, which can explain the observed pattern of sub-slab anomalies.

Supporting Information for "Impact of the Juan Fernandez ridge on the Pampean flat subduction inferred from full waveform inversion"

Yajian Gao[1,2], Xiaohui Yuan[1], Benjamin Heit[1], Frederik Tilmann[1,2],

Dirk-Philip van Herwaarden[3], Solvi Thrastarson[3], Andreas Fichtner[3], Bernd Schurr[1]

[1]GFZ German Research Centre for Geosciences, Potsdam, Germany

[2]Freie Universität Berlin, Berlin, Germany

[3]ETH, Zürich, Switzerland

Contents of this file

Texts S1, S2 and S3, Tables S1 and S2, Figures S1 to S26

S1: Model construction and inversion working flow

Long-wavelength surface topography from the EGM2008 Geoid (Pavlis et al., 2012) and Earth2014 global topography model (Hirt & Rexer, 2015) with Earth ellipticity according to WGS84 and Moho topography from Crust1.0 (Laske et al., 2013) are implemented by deforming the mesh grid vertically. The surface and Moho topography have been filtered with maximum angular order $lmax = 128$, equivalent to a spatial resolution of 155 km. In order to constrain the deep structure of the upper mantle, we initiate our inversion from long-period surface wave data at 60–120 s and progress in seven stages to a final period range of 12–120 s (see Table S2); the progressive extension to shorter periods mitigates the risk of falling into local minima. The model updates are driven by the Limited-Memory Broyden–Fletcher–Goldfarb–Shanno algorithm (L-BFGS Liu & Nocedal, 1989). We employ the Time-Frequency Phase Shift and Cross-Correlation-Coefficient misfits as misfit functions during stage I-V and VI-VII, respectively, following Gao et al. (2021) with the assistance of the *Large-scale Seismic Inversion Framework 2.0* (Krischer et al., 2015; Thrastarson et al., 2021). The detailed misfit evolution chart and histograms based on events and seismic traces are shown in Figure S4. Exemplary waveform fits from four events are illustrated in Figures S25-S28. More technical details about the inversion workflow can be found in Gao et al. (2021).

S2: Point-spreading tests

We analyse the resolution for the inversion and the trade-offs among the parameter types. In traditional ray theory tomography, the checkerboard test is popular and relatively robust with low computational costs, but it is computationally prohibitive for FWIs. In this study, we therefore approximate the Hessian-vector product $\mathbf{H}\delta\mathbf{m}$ for a test function $\delta\mathbf{m}$ (Fichtner & Trampert, 2011; Fichtner & Leeuwen, 2015; Zhu et al., 2015, 2017; Tao et al., 2018)

$$\mathbf{H}\delta\mathbf{m} = \mathbf{g}(\mathbf{m} + \delta\mathbf{m}) - \mathbf{g}(\mathbf{m}) \tag{1}$$

where $\mathbf{g}(\mathbf{m})$ denotes the summed gradient from the adjoint simulations for model $\mathbf{m}$, and $\mathbf{g}(\mathbf{m}+\delta\mathbf{m})$ indicates the gradient from the perturbed model $\mathbf{m}+\delta\mathbf{m}$.

If the synthetics from the final model provide a good fit of the observed data and the inversion thus has reached convergence, $\mathbf{H}\delta\mathbf{m}$ can be used to estimate the model resolution. Specifically, when the $\delta\mathbf{m}$ is nearly point-localised, the $\mathbf{H}\delta\mathbf{m}$ will be a linearised point-spread function.

In order to provide a visual representation of resolution throughout the model rather than just for a single model node, we perturbed our model by adding velocity perturbations $\delta\mathbf{m}$ in a three dimensional checkerboard pattern in the upper mantle made up of Gaussian spheres with $\pm 1\%$ maximum amplitude of the velocity for a specific depth and a Gaussian radius σ of 40 km. The horizontal and depth grid spacing of the Gaussian spheres are 2° and 100 km (Figure S17). We calculate $\mathbf{H}\delta\mathbf{m}$ for this anomaly pattern for V_{SV}, V_{SH} and isotropic V_P separately (Figure S17-S19).

Through the multi-parameter point-spread tests, we could confirm that the resolution for the inversion parameters is mostly confined to the top 400 km, although V_{SV} and isotropic V_P even show some ability to resolve the structure down to 460 km. The resolution of V_{SH} is confined to 360 km depth. Therefore, we could extend our interpretation on both of the isotropic V_S and V_P down to about 400 km.

To further quantitatively assess the resolution, we also present the normalised product of the perturbations $\delta\mathbf{m}$ and the resultant Hessian product $\mathbf{H}\delta\mathbf{m}$ within and between parameter classes (Figure S12-S14).

S3: Model comparison

In this section, we provide a simple comparison (Figure S17) between our model with (Ward et al., 2013). Although the shape of the recovered anomalies is sometimes quite different, the basic features can generally be found in both models. For example, the forearc has higher velocities than the main volcanic arc, indicating colder temperatures. Importantly, in the middle crust (20 km) only moderately low velocities are found from 29°S to 32°S and spread over a wider distance in EW-direction, compared to the segments north and south with stronger anomalies confined to the active volcanic arc. In general, the anomalies imaged by us tend to be more focused and with larger amplitudes, compared to Ward et al. (2013).

References

Albuquerque Seismological Laboratory (ASL)/USGS. (1988). *Global Seismograph Network (GSN - IRIS/USGS).* International Federation of Digital Seismograph Networks. doi: https://doi.org/10.7914/SN/IU

Albuquerque Seismological Laboratory (ASL)/USGS. (1993). *Global Telemetered Seismograph Network (USAF/USGS).* International Federation of Digital Seismograph Networks. doi: https://doi.org/10.7914/SN/GT

Asch, G., Heit, B., & Yuan, X. (2002). *The ReFuCA project: Receiver Functions Central Andes.* GFZ Data Services.

Beck, L., Susan, & Terry, W. (2000). *Slab Geometry in the Southern Andes.* International Federation of Digital Seismograph Networks. Retrieved from `http://www.fdsn.org/doi/10.7914/SN/YC_2000` doi: https://doi.org/10.7914/SN/YC_2000

Beck, L., Susan, & Zandt, G. (2007). *Lithospheric Structure and Deformation of the Flat Slab Region of Argentina.* International Federation of Digital Seismograph Networks. doi: https://doi.org/10.7914/SN/ZL_2007

Dziewonski, A. M., & Anderson, D. L. (1981). Preliminary reference Earth model. *Physics of the Earth and Planetary Interiors*, *25*(4), 297 - 356. doi: https://doi.org/10.1016/0031-9201(81)90046-7

Fichtner, A., & Leeuwen, T. v. (2015). Resolution analysis by random probing. *Journal of Geophysical Research: Solid Earth*, *120*(8), 5549-5573. doi: https://doi.org/10.1002/2015JB012106

Fichtner, A., & Trampert, J. (2011). Resolution analysis in full waveform inversion. *Geophysical Journal International*, *187*(3), 1604–1624. doi: https://doi.org/10.1111/j.1365-246X.2011.05218.x

Gao, Y., Tilmann, F., van Herwaarden, D.-P., Thrastarson, S., Fichtner, A., Heit, B., . . . Schurr, B. (2021). Full Waveform Inversion beneath the Central Andes: Insight into the dehydration of the Nazca slab and delamination of the back-arc lithosphere. *Journal of Geophysical Research: Solid Earth*, *126*(7), e2021JB021984. doi: https://doi.org/10.1029/2021JB021984

GFZ, & CNRS-INSU. (2006). *IPOC Seismic Network.* Integrated Plate boundary Observatory Chile - IPOC. doi: https://doi.org/10.14470/PK615318

Hayes, G. P., Moore, G. L., Portner, D. E., Hearne, M., Flamme, H., Furtney, M., & Smoczyk, G. M. (2018). Slab2, a comprehensive subduction zone geometry model. *Science*, *362*(6410), 58–61. doi: https://doi.org/10.1126/science.aat4723

Heit, B., Yuan, X., Kind, R., & Asch, G. (2007). *Lithospheric dynamics in the southernmost Andean Plateau (PUDEL).* GFZ Data Services. doi: https://doi.org/10.14470/7O092361

Hersh, Gilbert. (2008). *Eastern Sierras Pampeanas, Lithospheric Structure above the variably dipping Nazca Slab.* International Federation of Digital Seismograph Networks. doi: https://doi.org/10.7914/SN/XH_2008

Hirt, C., & Rexer, M. (2015). Earth2014: 1 arc-min shape, topography, bedrock and ice-sheet models – Available as gridded data and degree-10,800 spherical harmonics. *International Journal of Applied Earth Observation and Geoinformation*, *39*, 103 - 112. doi: https://doi.org/10.1016/j.jag.2015.03.001

IPGP, & EOST. (1982). *GEOSCOPE, French Global Network of broad band seismic stations.* Institut de physique du globe de Paris (IPGP), Université de Paris. Retrieved from `http://geoscope.ipgp.fr/networks/detail/G/` doi: https://doi.org/10.18715/GEOSCOPE.G

Krischer, L., Fichtner, A., Zukauskaite, S., & Igel, H. (2015). Large?scale seismic inversion framework. *Seismological Research Letters*, *86*(4), 1198. Retrieved from `http://dx.doi.org/10.1785/0220140248` doi: https://doi.org/10.1785/0220140248

Lange, D., Cembrano, J., & Sielfeld, G. (2019). *Crustal Seismicity along for the Southern Andes Volcanic Zone (LOFS).* GFZ Data Services. doi: https://doi.org/10.14470/8U7569253520

Laske, G., Masters, G., Ma, Z., & Pasyanos, M. (2013). Update on CRUST1. 0—A 1-degree global model of Earth's crust. In *Geophys. Res. Abstracts, 15, Abstract EGU2013-2658.*

Liu, D. C., & Nocedal, J. (1989, Aug 01). On the limited memory bfgs method for large scale optimization. *Mathematical Programming*, *45*(1), 503–528. Retrieved from https://doi.org/10.1007/BF01589116 doi: 10.1007/BF01589116

Pavlis, N. K., Holmes, S. A., Kenyon, S. C., & Factor, J. K. (2012). The development and evaluation of the Earth Gravitational Model 2008 (EGM2008). *Journal of Geophysical Research: Solid Earth*, *117*(B4). doi: https://doi.org/10.1029/2011JB008916

Rietbrock, A., Haberland, C., Bataille, K., Lange, D., & Dahm, T. (2004). *TIPTEQ-Temporary seismological network (North) (2004/2005).* GFZ Data Services. doi: https://doi.org/10.14470/MJ7559637482

Ritsema, J., van Heijst, H. J., & Woodhouse, J. H. (1999). Complex shear wave velocity structure imaged beneath Africa and Iceland. *Science*, *286*(5446), 1925–1928. doi: https://doi.org/10.1126/science.286.5446.1925

Rivadeneyra-Vera, C., Bianchi, M., Assumpção, M., Cedraz, V., Julià, J., Rodríguez, M., ... others (2019). An updated crustal thickness map of central South America based on receiver function measurements in the region of the Chaco, Pantanal, and Paraná Basins, southwestern Brazil. *Journal of Geophysical Research: Solid Earth*, *124*(8), 8491–8505. doi: https://doi.org/10.1029/2018JB016811

Sandvol, E., & Brown, L. (2007). *SLIP—Seismic Lithospheric Imaging of the Puna Plateau.* International Federation of Digital Seismograph Networks. doi: https://doi.org/10.7914/SN/X6_2007

Schurr, B., Asch, G., & Wigger, P. (1997). *PUNA Project.* GFZ Data Services. doi: https://doi.org/10.14470/MO6442843258

Sippl, C., Moreno, M., & Benavente, R. (2020). Microseismicity appears to outline highly coupled regions on the Central Chile megathrust. *EarthArXiv*. doi: https://doi.org/

10.31223/X56S3B

Steve Roecker, R. R. (2010). *RAMP response for 2010 earthquake.* International Federation of Digital Seismograph Networks. Retrieved from `http://www.fdsn.org/doi/10.7914/SN/XY_2010` doi: https://doi.org/10.7914/SN/XY_2010

Tao, K., Grand, S. P., & Niu, F. (2018). Seismic Structure of the Upper Mantle Beneath Eastern Asia From Full Waveform Seismic Tomography. *Geochemistry, Geophysics, Geosystems*, *19*(8), 2732-2763. doi: https://doi.org/10.1029/2018GC007460

Thrastarson, S., van Herwaarden, D. P., Krischer, L., & Fichtner, A. (2021). LASIF: Large-scale Seismic Inversion Framework, an updated version. doi: https://doi.org/10.31223/X5NC84

Thurber, C. (2015). *Laguna del Maule seismic imaging.* International Federation of Digital Seismograph Networks. doi: https://doi.org/10.7914/SN/ZR_2015

Universidad De Chile. (2013). *Red Sismologica Nacional.* International Federation of Digital Seismograph Networks. doi: https://doi.org/10.7914/SN/C1

Vilotte, J., et al. (2011). *Seismic network XS: CHILE MAULE aftershock temporary experiment (RESIF-SISMOB).* RESIF-Réseau Sismologique et géodésique Français. doi: https://doi.org/10.15778/RESIF.XS2010

Waite, G. P. (2010). *An Integrated Analysis of Low-Frequency Seismicity at Villarrica Volcano, Chile.* International Federation of Digital Seismograph Networks. doi: https://doi.org/10.7914/SN/YM_2010

Ward, K. M., Porter, R. C., Zandt, G., Beck, S. L., Wagner, L. S., Minaya, E., & Tavera, H. (2013). Ambient noise tomography across the Central Andes. *Geophysical Journal*

International, *194*(3), 1559-1573. doi: https://doi.org/10.1093/gji/ggt166

Zhu, H., Bozdağ, E., & Tromp, J. (2015). Seismic structure of the European upper mantle based on adjoint tomography. *Geophysical Journal International*, *201*(1), 18–52. doi: https://doi.org/10.1093/gji/ggu492

Zhu, H., Komatitsch, D., & Tromp, J. (2017). Radial anisotropy of the North American upper mantle based on adjoint tomography with USArray. *Geophysical Journal International*, *211*(1), 349-377. doi: https://doi.org/10.1093/gji/ggx305

Table S1. Seismic Network information

Code	Data Center	start	end	reference
C	IRISDMC	2007	2009	Chilean National Seismic Network
$C1$	IRISDMC	2012	-	Universidad De Chile (2013)
CX	GEOFON	2006	-	GFZ and CNRS-INSU (2006)
GT	IRISDMC	1993	-	Albuquerque Seismological Laboratory (ASL)/USGS (1993)
IU	IRISDMC	1988	-	Albuquerque Seismological Laboratory (ASL)/USGS (1988)
WA	IRISDMC	2011	-	West Central Argentina Network
$2B$	GEOFON	2007	2009	Heit et al. (2007)
$3A$	IRISDMC	2010	2012	Maule Aftershock Deployment (UK)
$3H$	GEOFON	2014	2015	Lange et al. (2019)
G	IPGP	1982	-	IPGP and EOST (1982)
$X6$	IRISDMC	2007	2009	Sandvol and Brown (2007)
XH	IRISDMC	2008	2010	Hersh, Gilbert (2008)
XS	RESIF	2010	2011	Vilotte et al. (2011)
XY	IRISDMC	2010	2010	Steve Roecker (2010)
YC	IRISDMC	2002	2002	Beck and Terry (2000)
YM	IRISDMC	2010	2012	Waite (2010)
ZA	GEOFON	2002	2004	Asch et al. (2002)
ZB	GEOFON	1997	1997	Schurr et al. (1997)
ZE	GEOFON	2010	2011	Maule Aftershock Survey-GFZ
ZL	IRISDMC	2007	2009	Beck and Zandt (2007)
ZP	GEOFON	1999	2001	ISSA Southern Andes
ZQ	GEOFON	2004	2005	Cerro Blanco Project Central Andes
ZR	IRISDMC	2015	2018	Thurber (2015)
ZW	GEOFON	2005	2005	Rietbrock et al. (2004)

Table S2. Overview of inversion stages. TF: Time Frequency, CCC: Cross Correlation Coefficient

No.	Periods	It.	Simulation time	Events	Windows	Misfit
I	60–120 s	5	450 s	71	7785	TF
II	40–120 s	7	450 s	93	10211	TF
III	30–100 s	7	450 s	93	12497	TF
IV	20–100 s	11	450 s	93	12497	TF
V	20–100 s	7	450 s	110	28399	TF
VI	15–100 s	9	450 s	120	61516	CCC
VII	12–100 s	8	450 s	139	74751	CCC

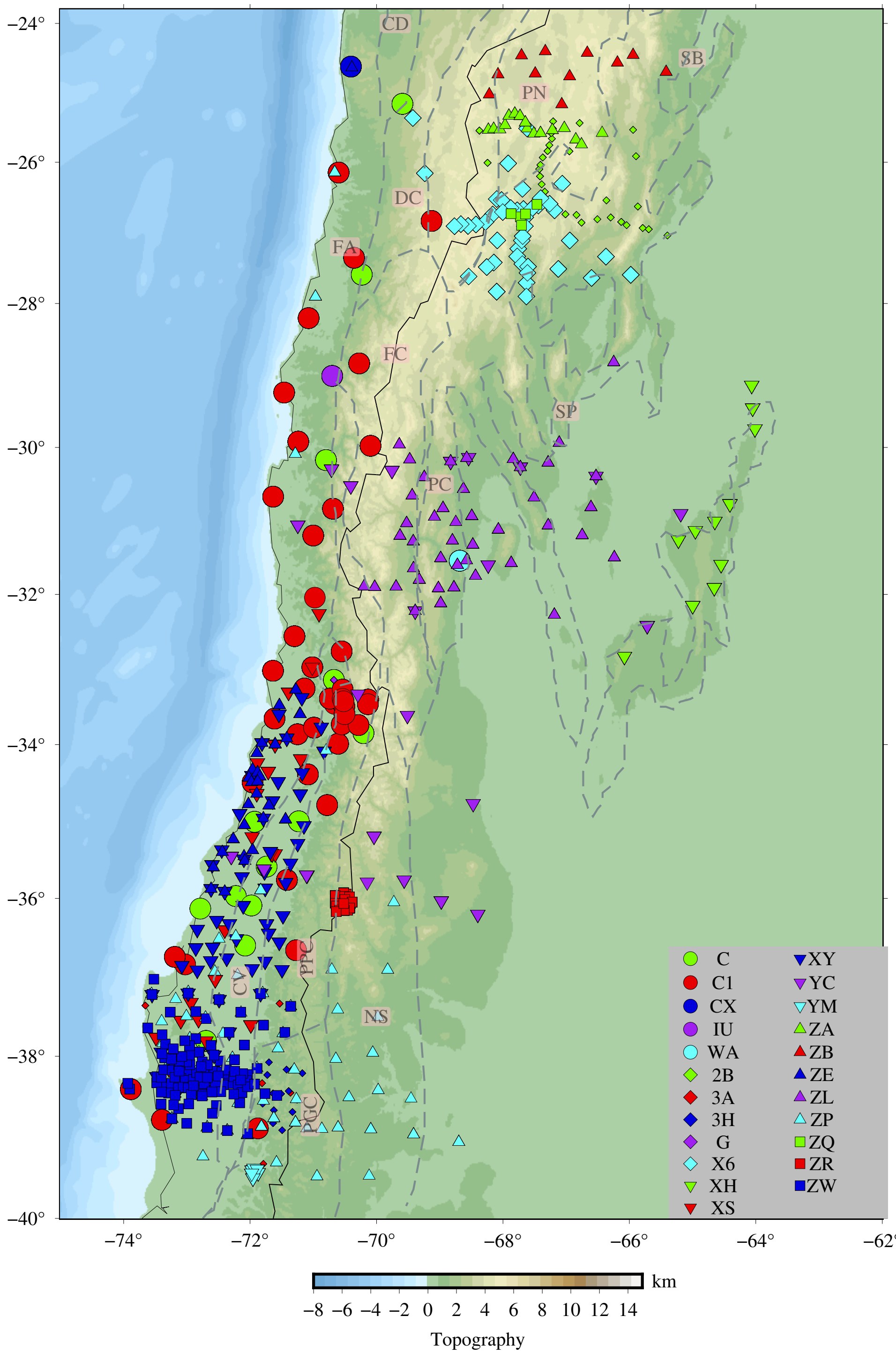

Figure S1. Map showing seismic stations of individual networks used in the study with circles marking the permanent stations. Detailed information about the networks is given in Table S1

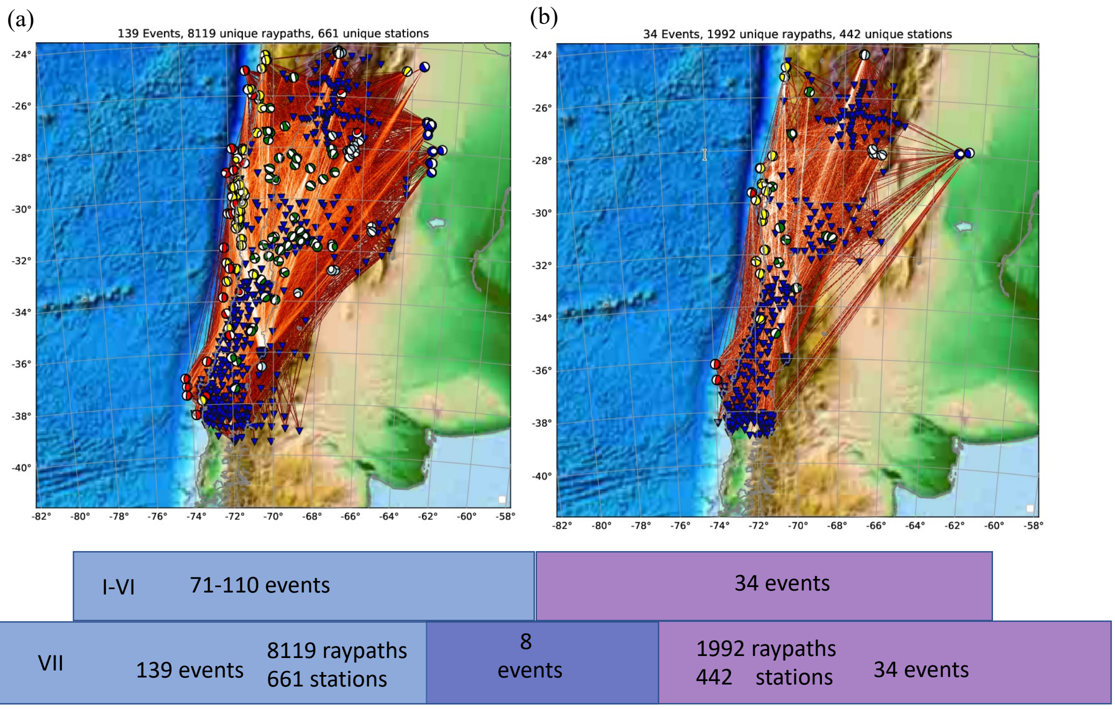

Figure S2. (a) Earthquakes, stations and ray-paths used for the inversion. (b) Earthquakes, stations and ray-paths for the validation dataset. 8 earthquakes are overlapped between the inversion data set and validation data set in the final inversion stage (VII). The waveforms in the validation dataset were not used in the inversion, but instead used to evaluate improvement of the model and avoid overfitting. See Fig. S4 for a comparison of fit improvements in inversion and validation dataset.

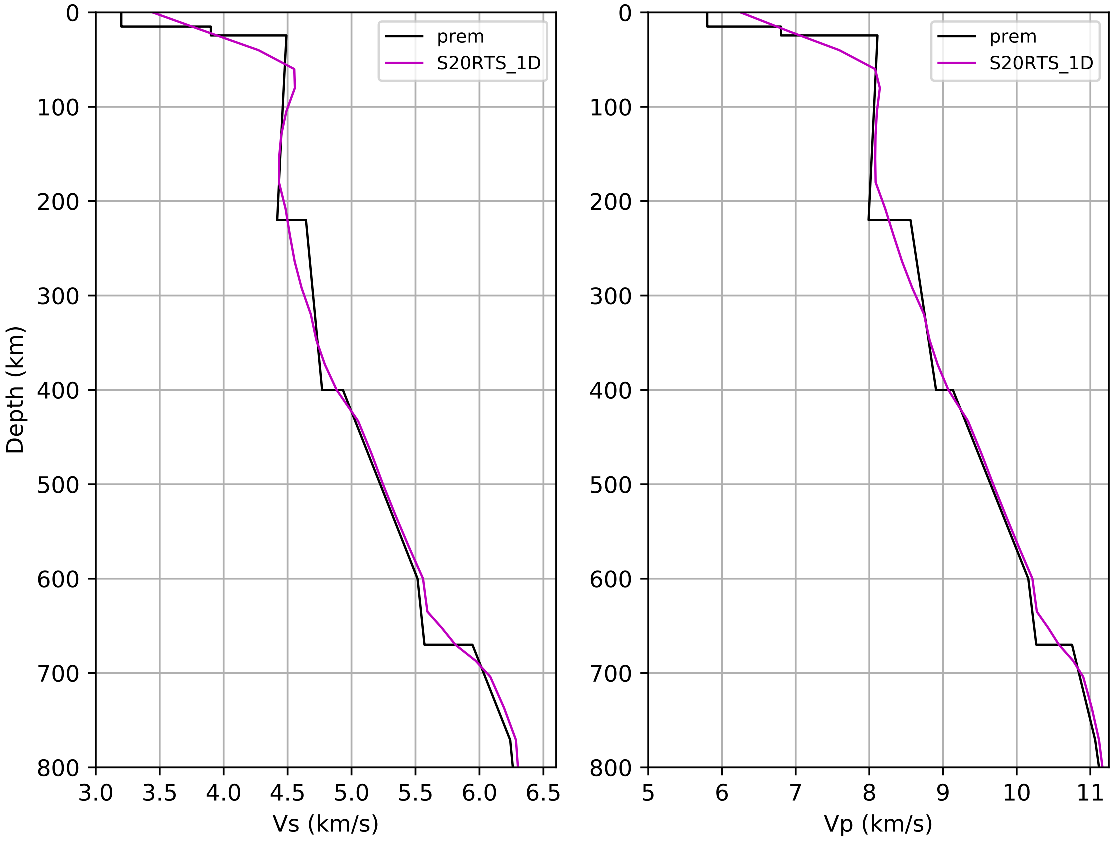

Figure S3. The reference 1D model derived from the depth-averaged initial S20RTS (Ritsema et al., 1999) model, compared with isotropic PREM (Dziewonski & Anderson, 1981).

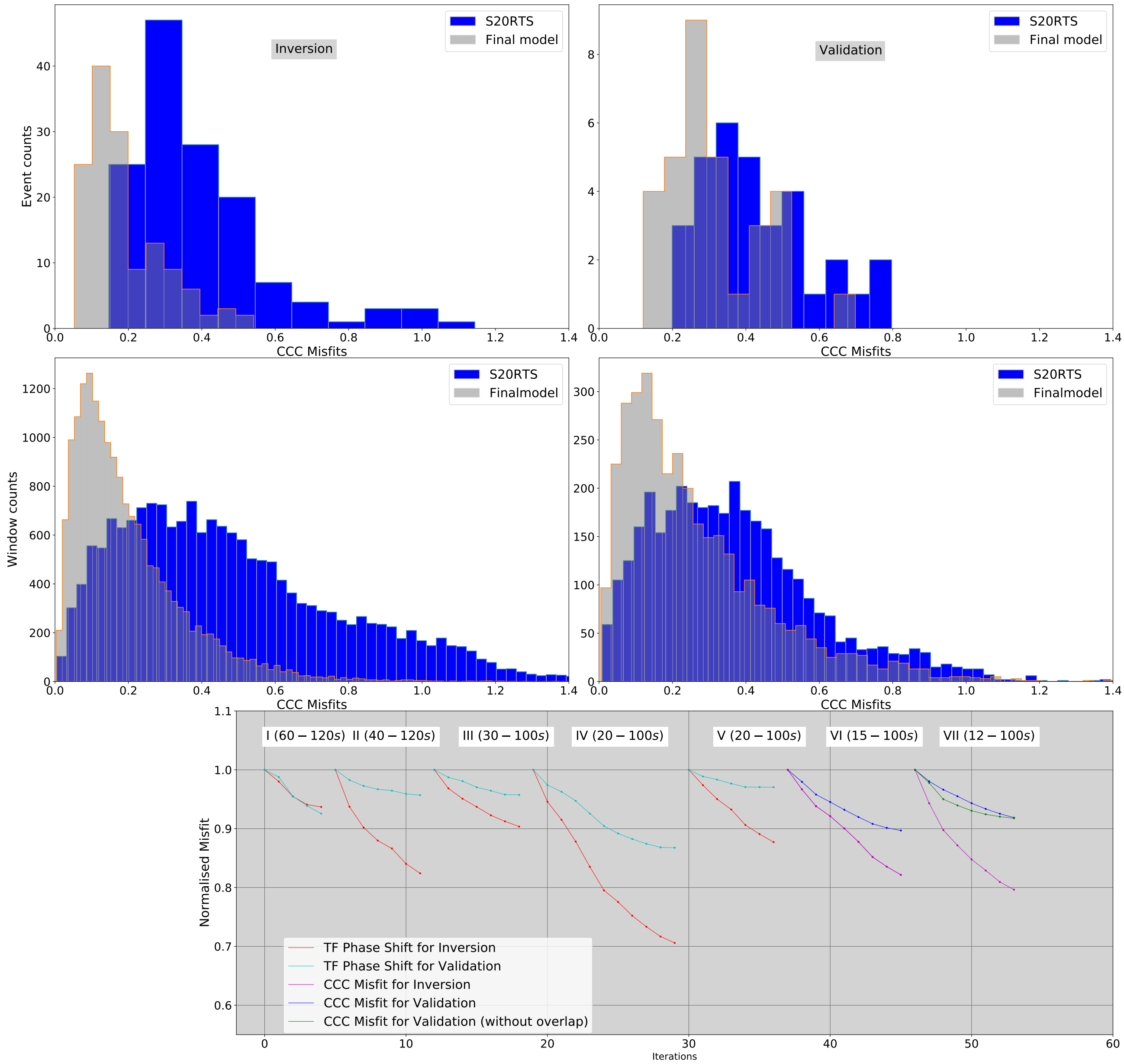

Figure S4. Top: Histogram of average cross corrrelation coefficient (CCC) misfits for each event for the starting model and after the final iteration; the left column shows the inversion, the right column the validation data set. Middle: Histogram of CCC misfits for each trace; Lower: Misfit evolution with iterations. See Fig. S2 for more details on inversion and validation dataset.

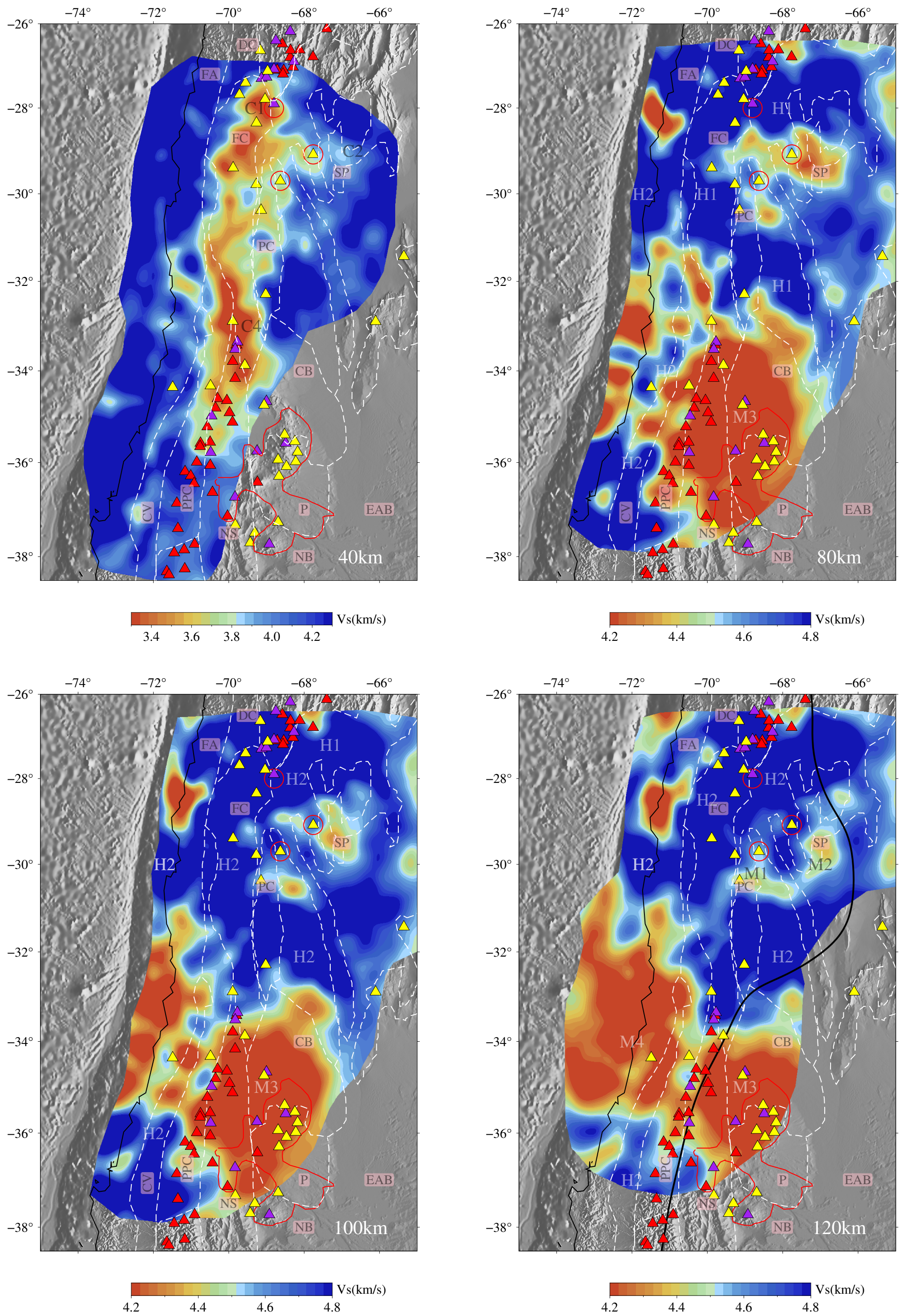

Figure S5. Horizontal slices for isotropic V_S model at 40 km, 80 km, 100 km and 120 km depth.

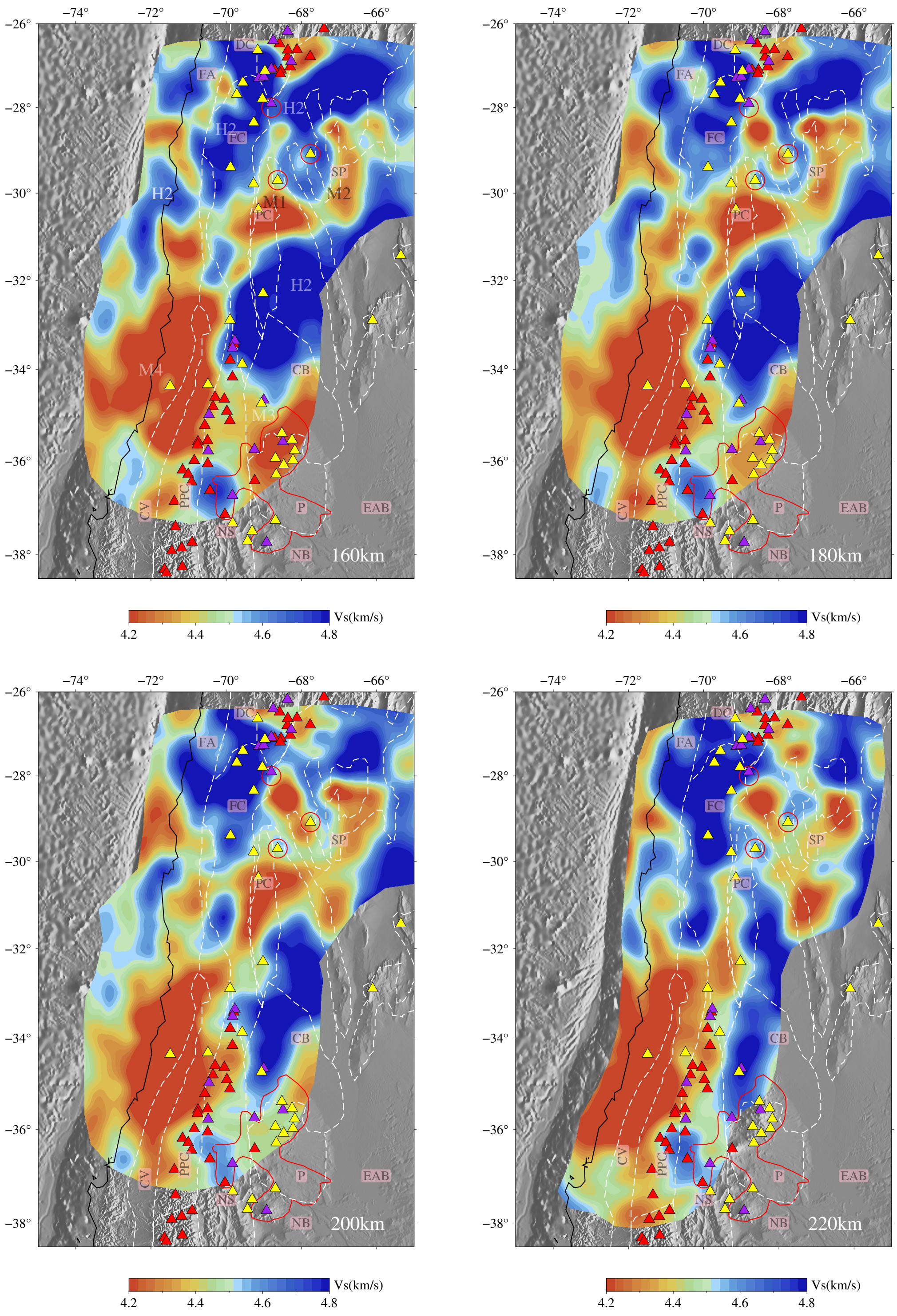

Figure S6. Horizontal slices for isotropic V_S model at 160 km, 180 km, 200 km and 220 km depth.

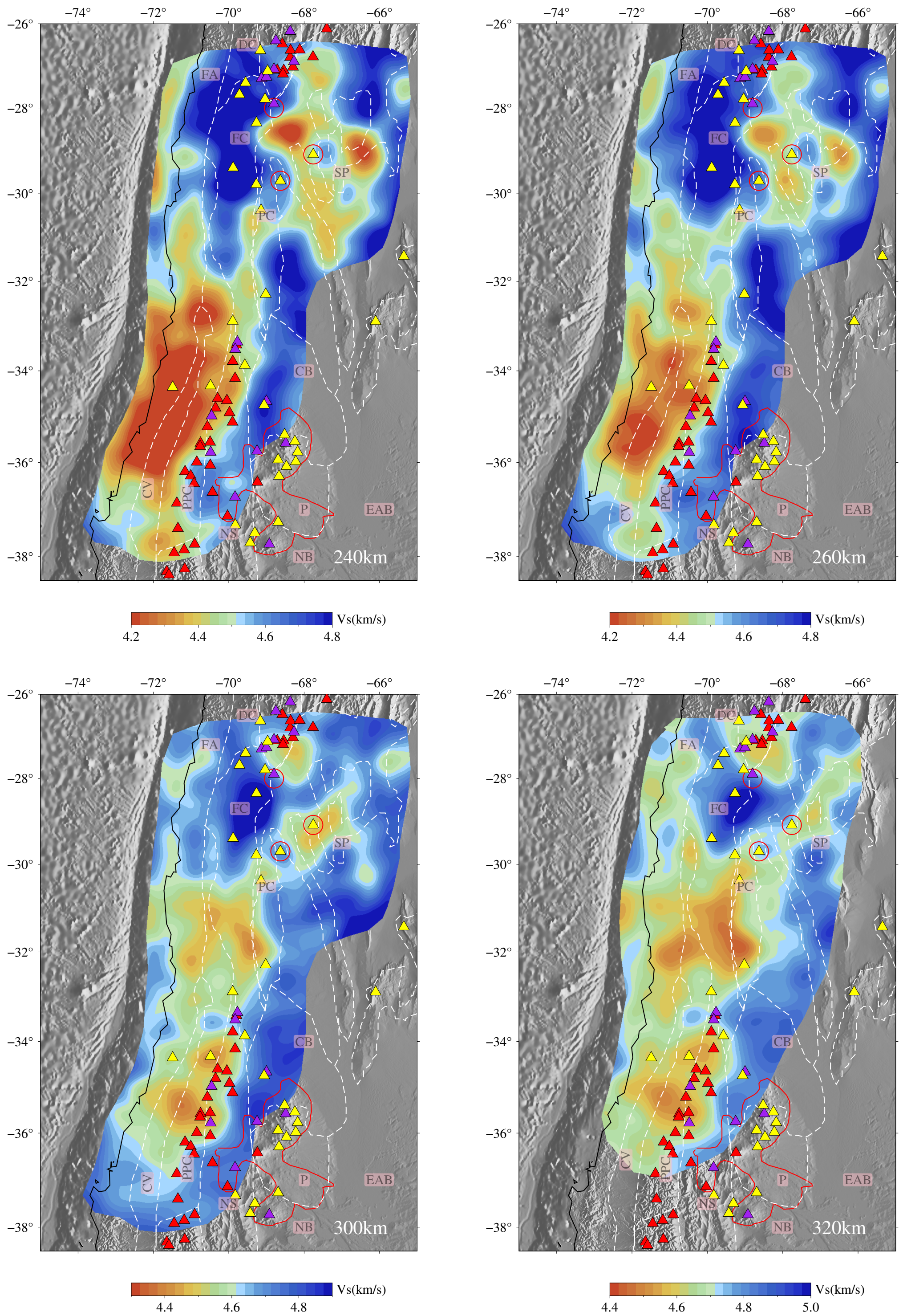

Figure S7. Horizontal slices for isotropic V_S model at 240 km, 260 km, 300km and 320 km depth.

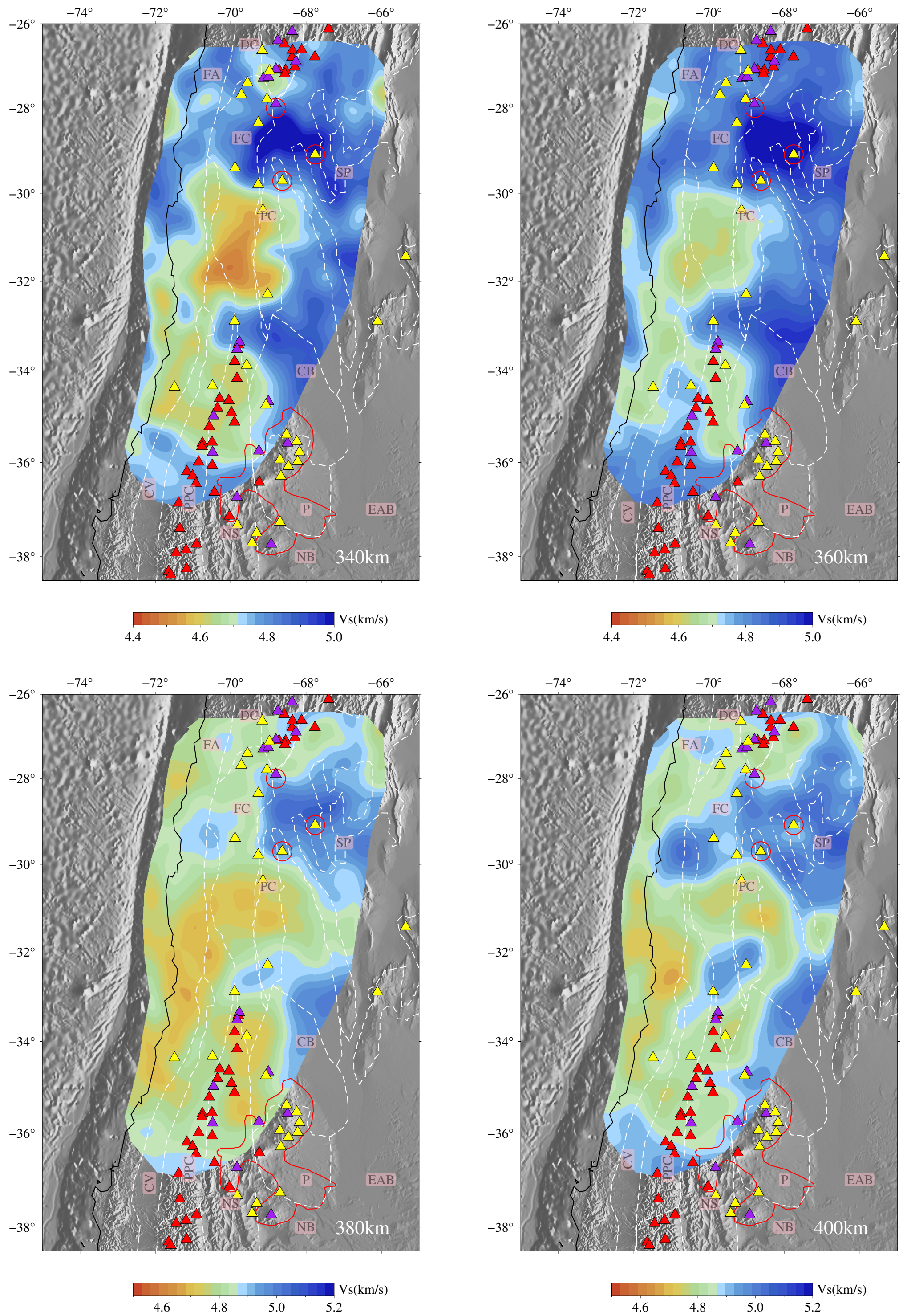

Figure S8. Horizontal slices for isotropic V_S model at 340 km, 360 km, 380 km and 400 km depth.

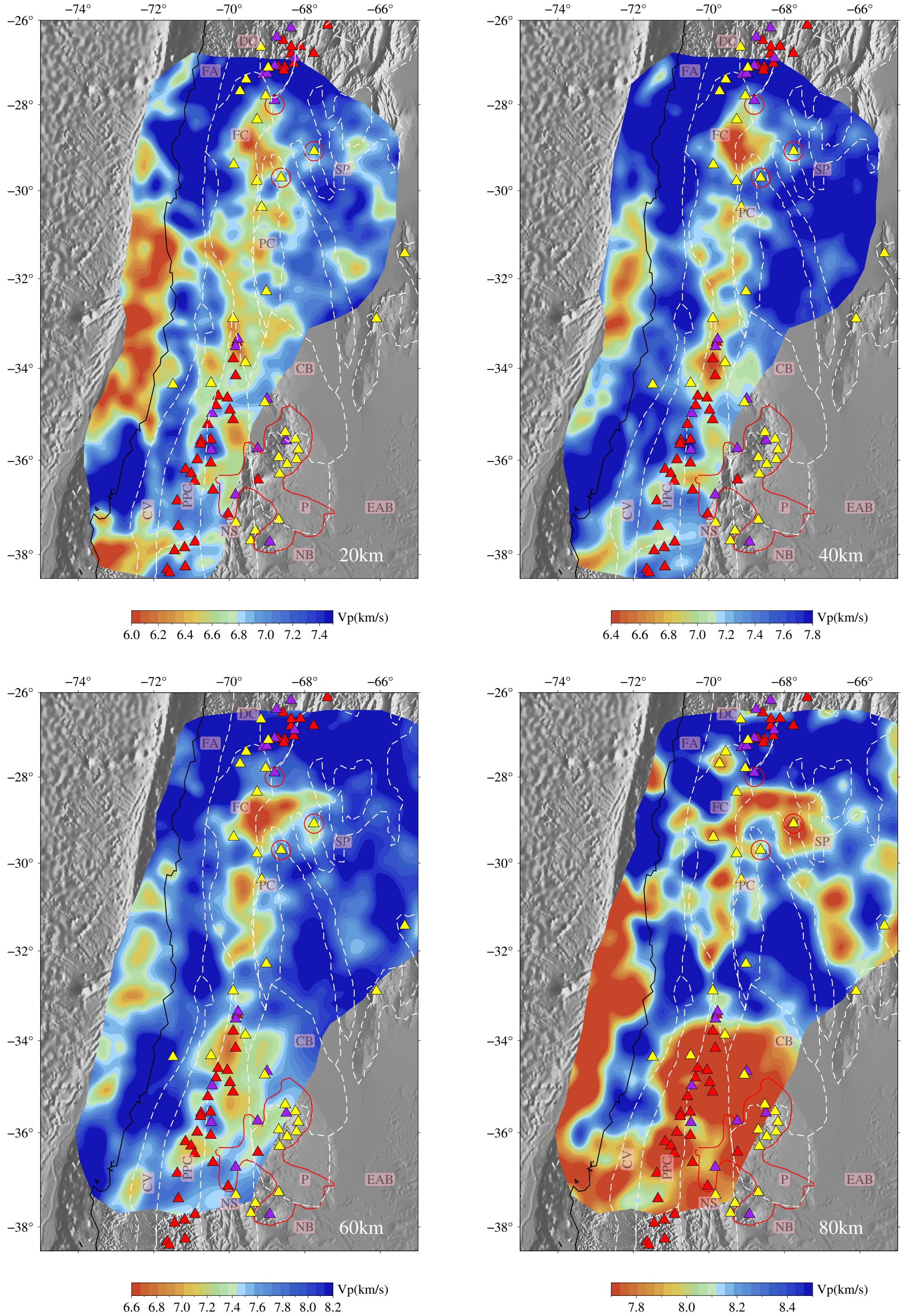

Figure S9. Horizontal slices for isotropic V_P model at 20 km, 40 km, 60 km and 80 km depth.

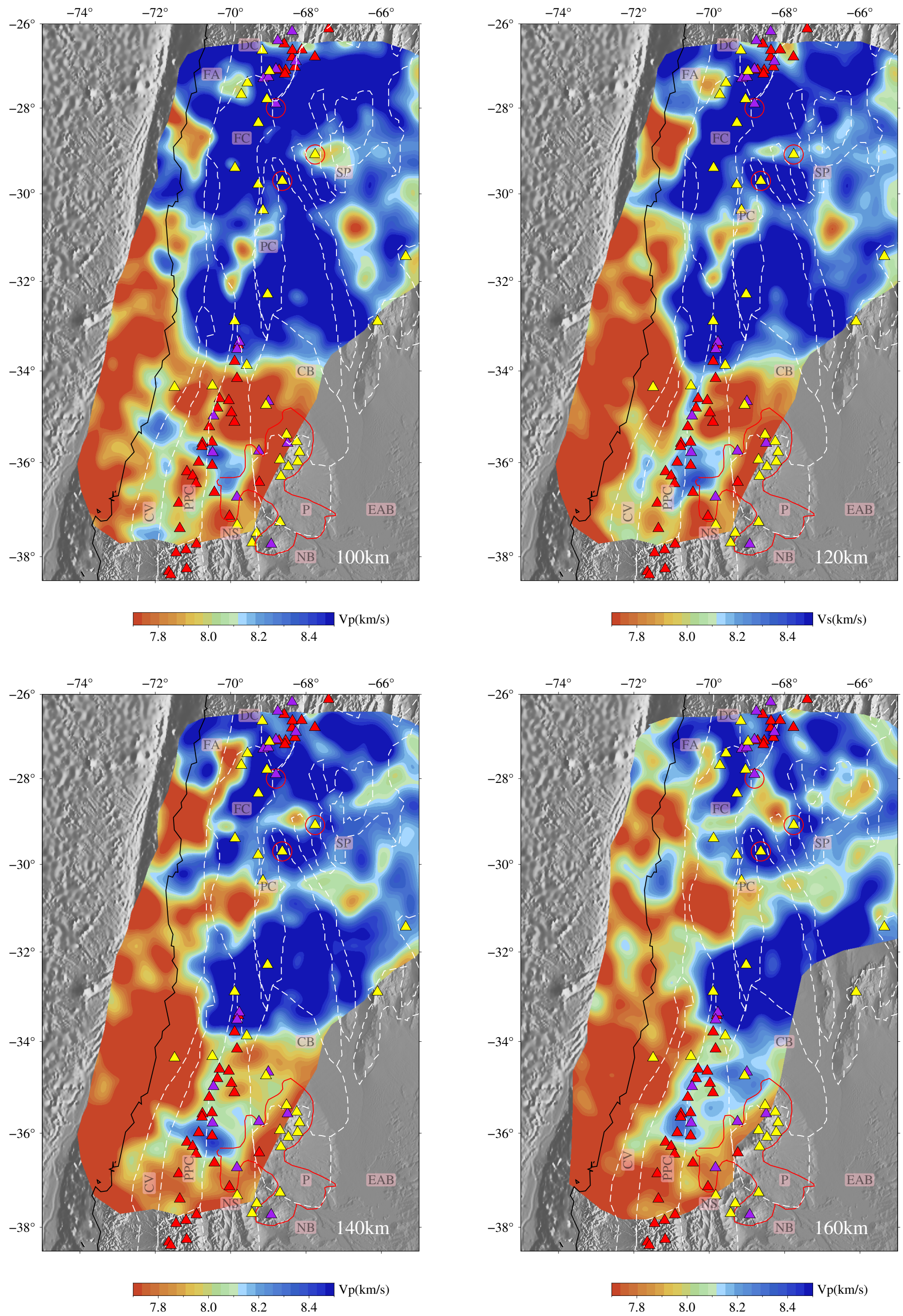

Figure S10. Horizontal slices for isotropic V_P model at 100 km, 120 km, 140 km and 160 km depth.

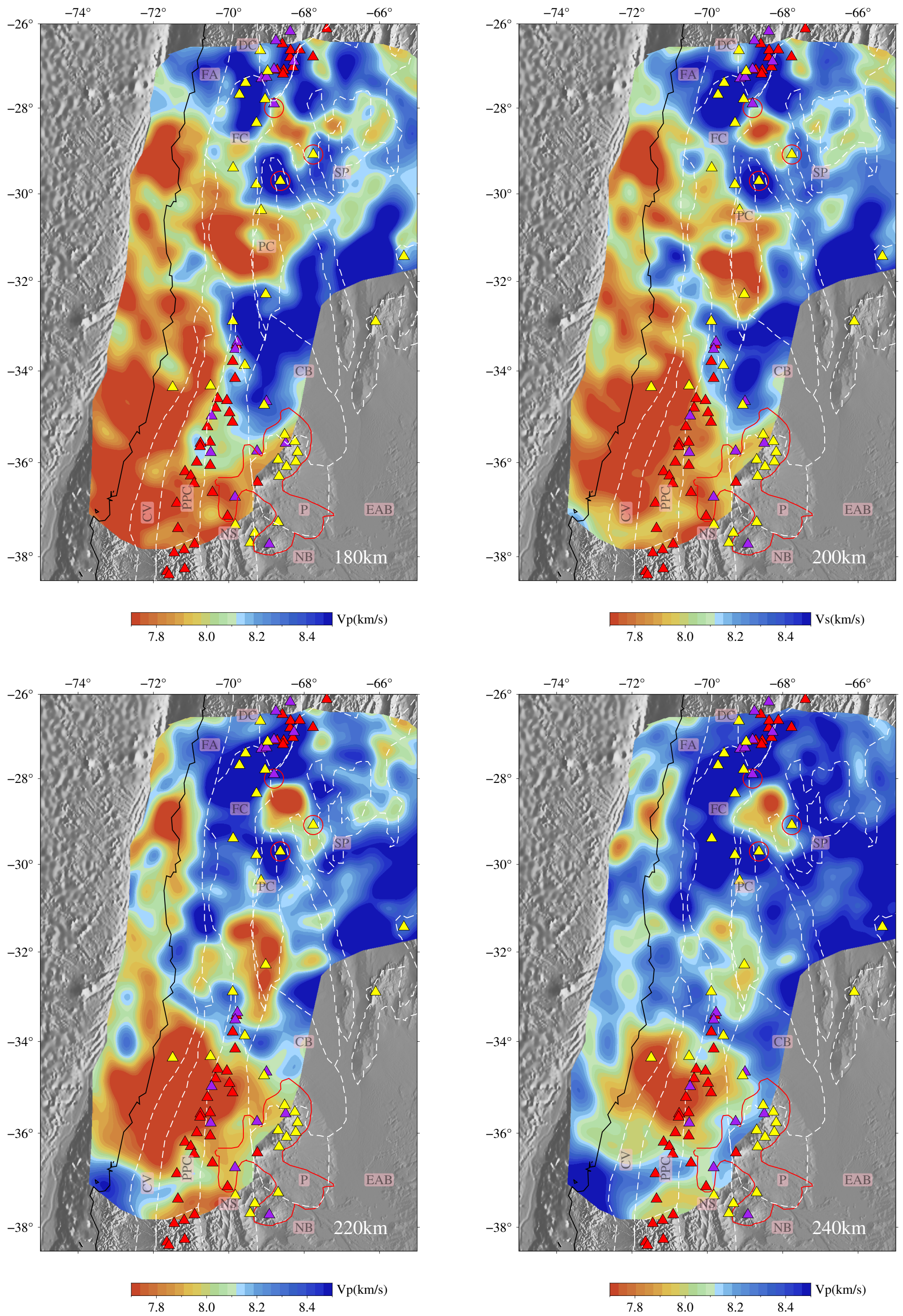

Figure S11. Horizontal slices for isotropic V_P model at 180 km, 200 km, 220 km and 240 km depth.

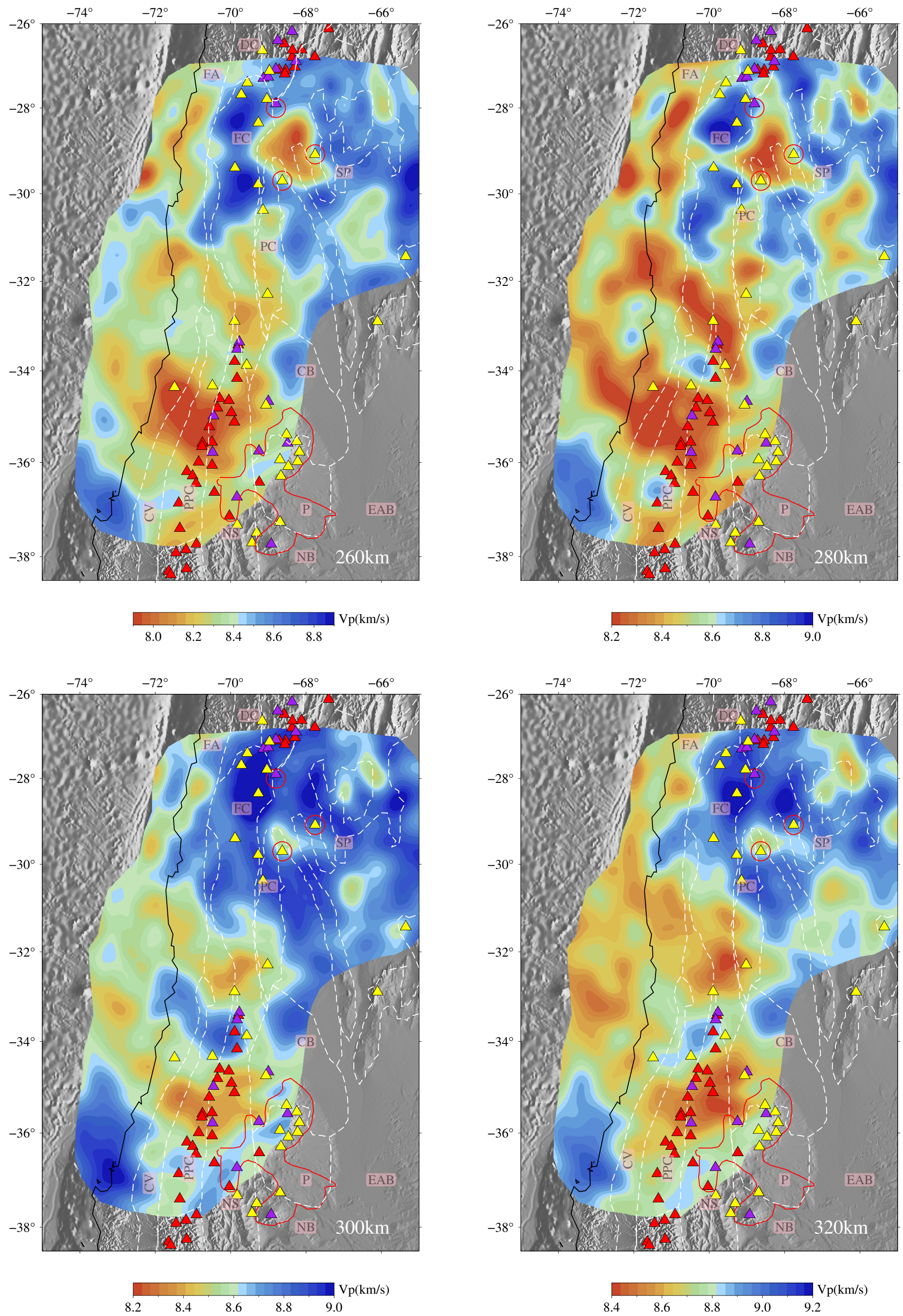

Figure S12. Horizontal slices for isotropic V_P model at 260 km, 280 km, 300 km and 320 km depth.

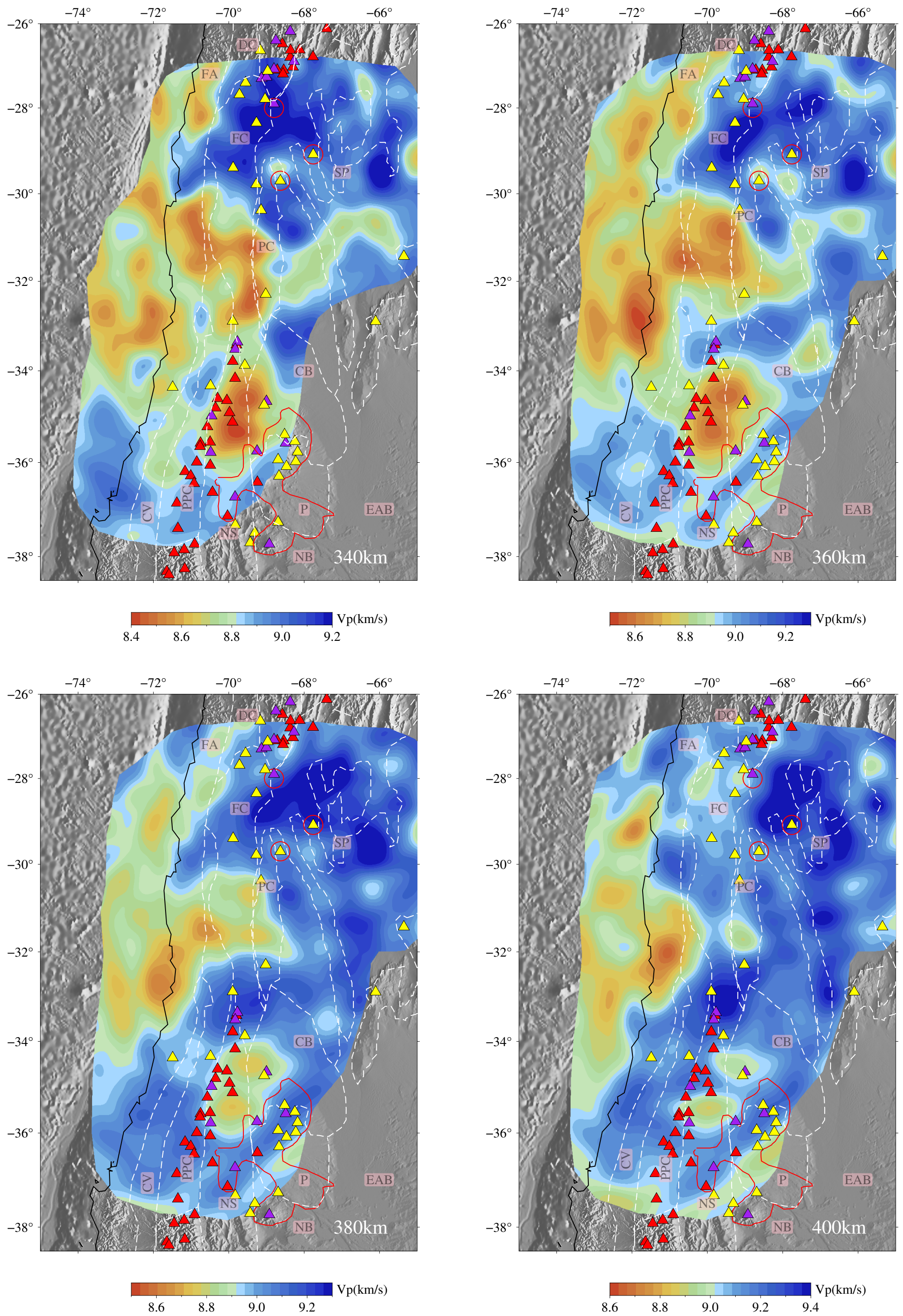

Figure S13. Horizontal slices for isotropic V_P model at 340 km, 360 km, 380 km and 400 km depth.

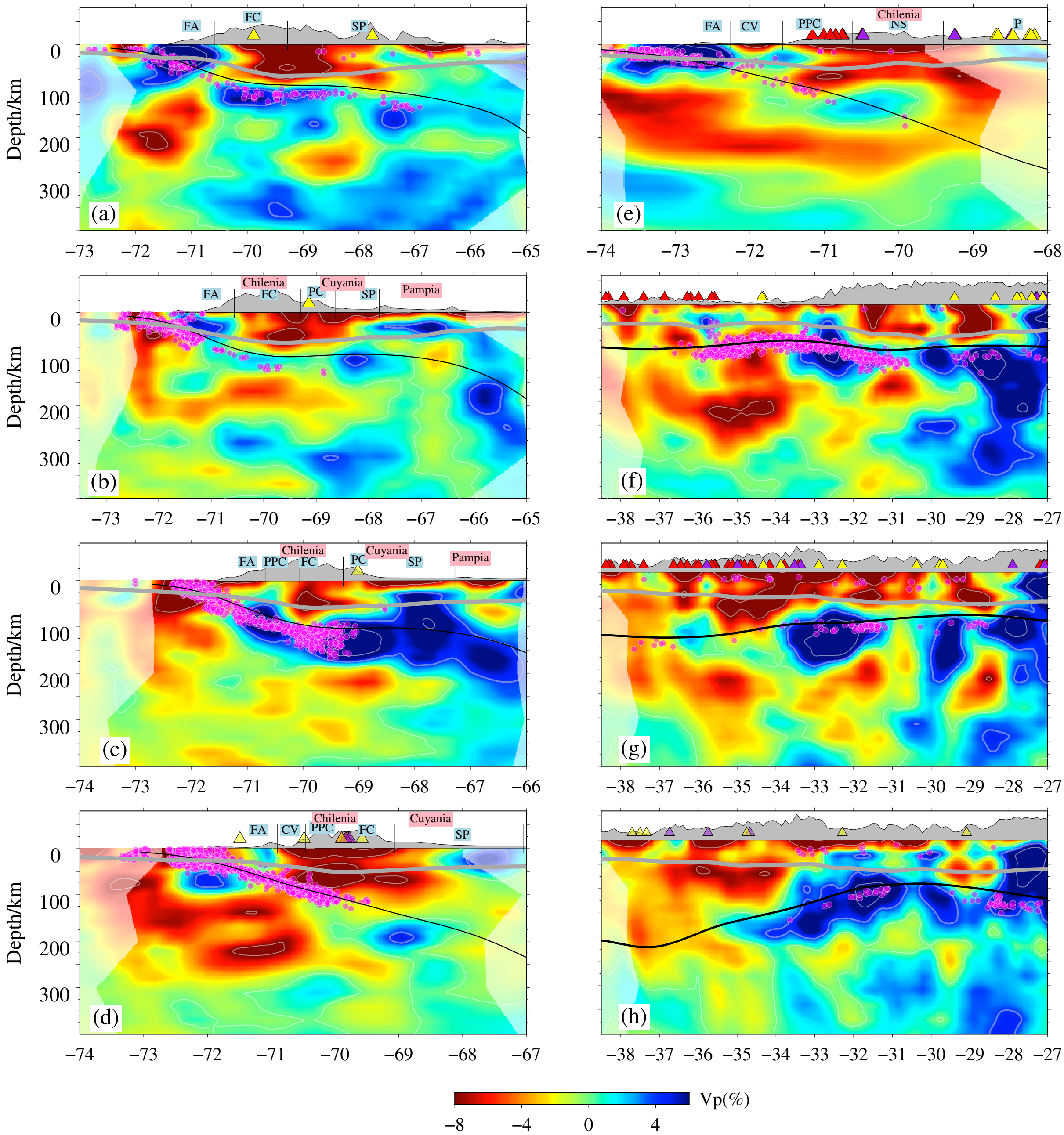

Figure S14. Cross-sections of isotropic V_p perturbations relative to the reference 1D V_p. The positions for the cross sections are defined in Figure 2(d) (see main text). Thick solid gray lines denote the continental Moho (Rivadeneyra-Vera et al., 2019) and thin solid black lines denote the slab contour from Slab 2.0 (Hayes et al., 2018). Magenta dots in b-d denote the seismicity relocated by Sippl et al. (2020) and in other profiles are retrieved from ISC-EHB catalog.

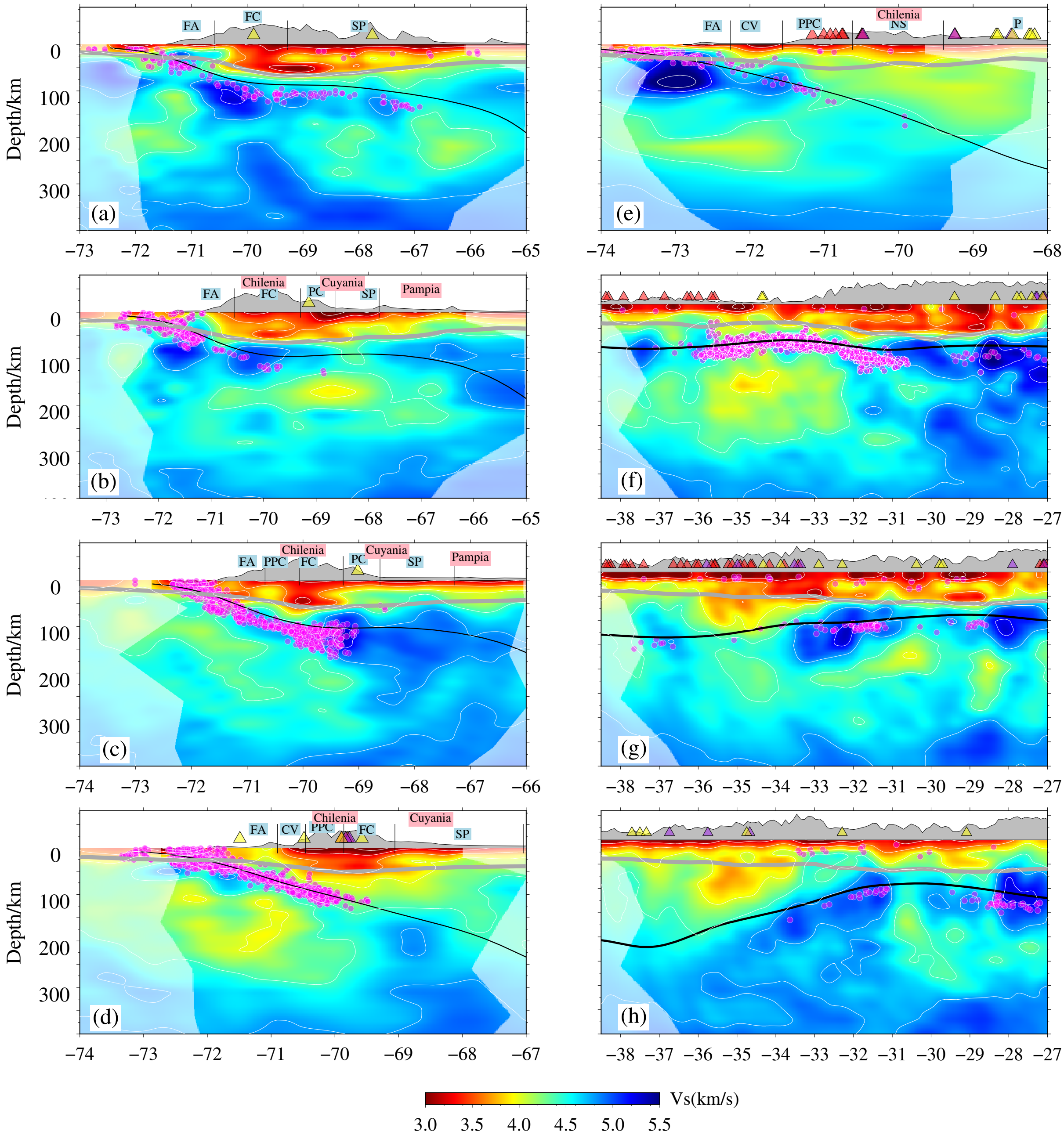

Figure S15. Isotropic absolute V_S cross-sections. For other figure elements see Fig. S14.

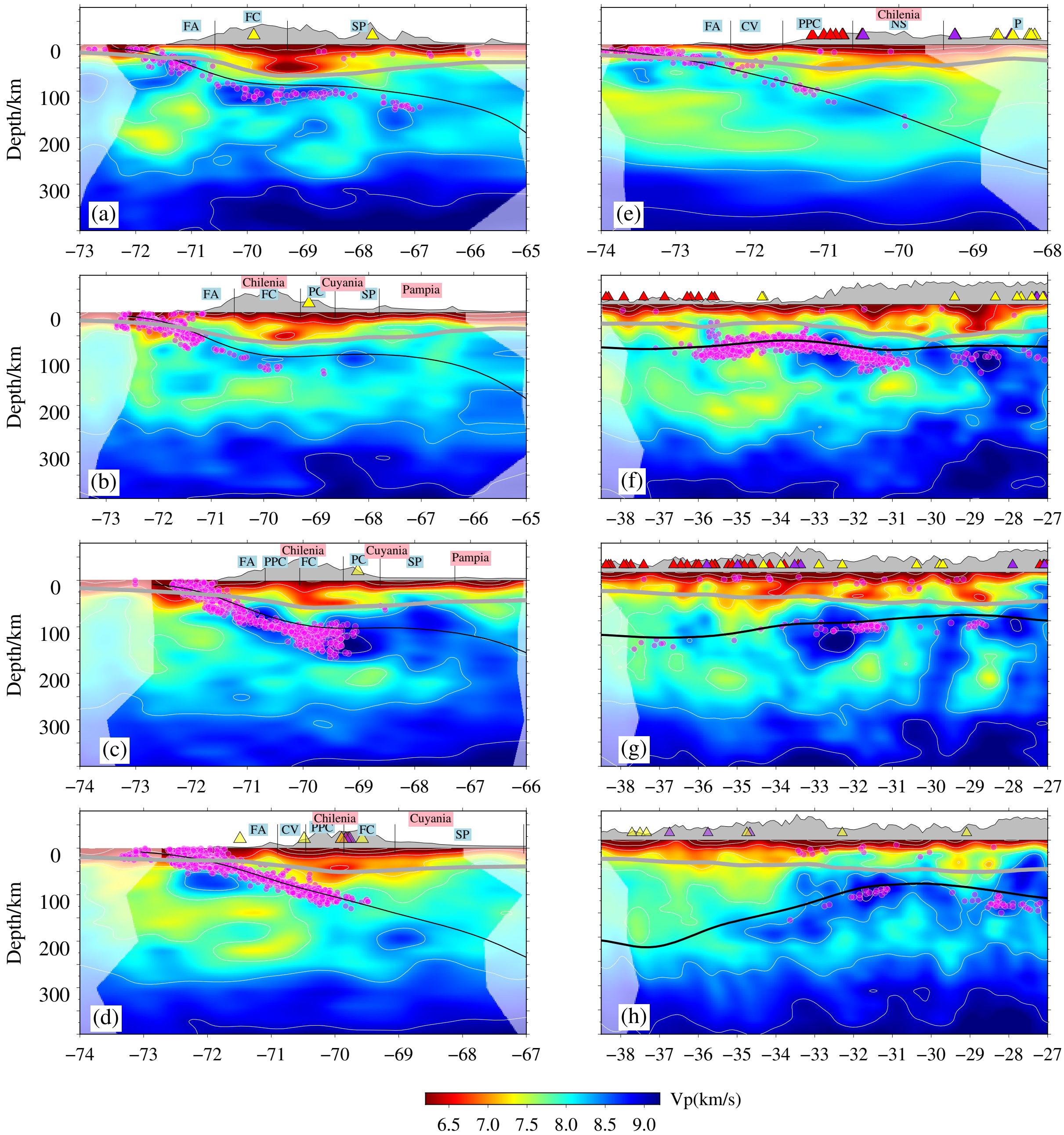

Figure S16. Isotropic absolute V_P cross-sections. For other figure elements see Fig. S14

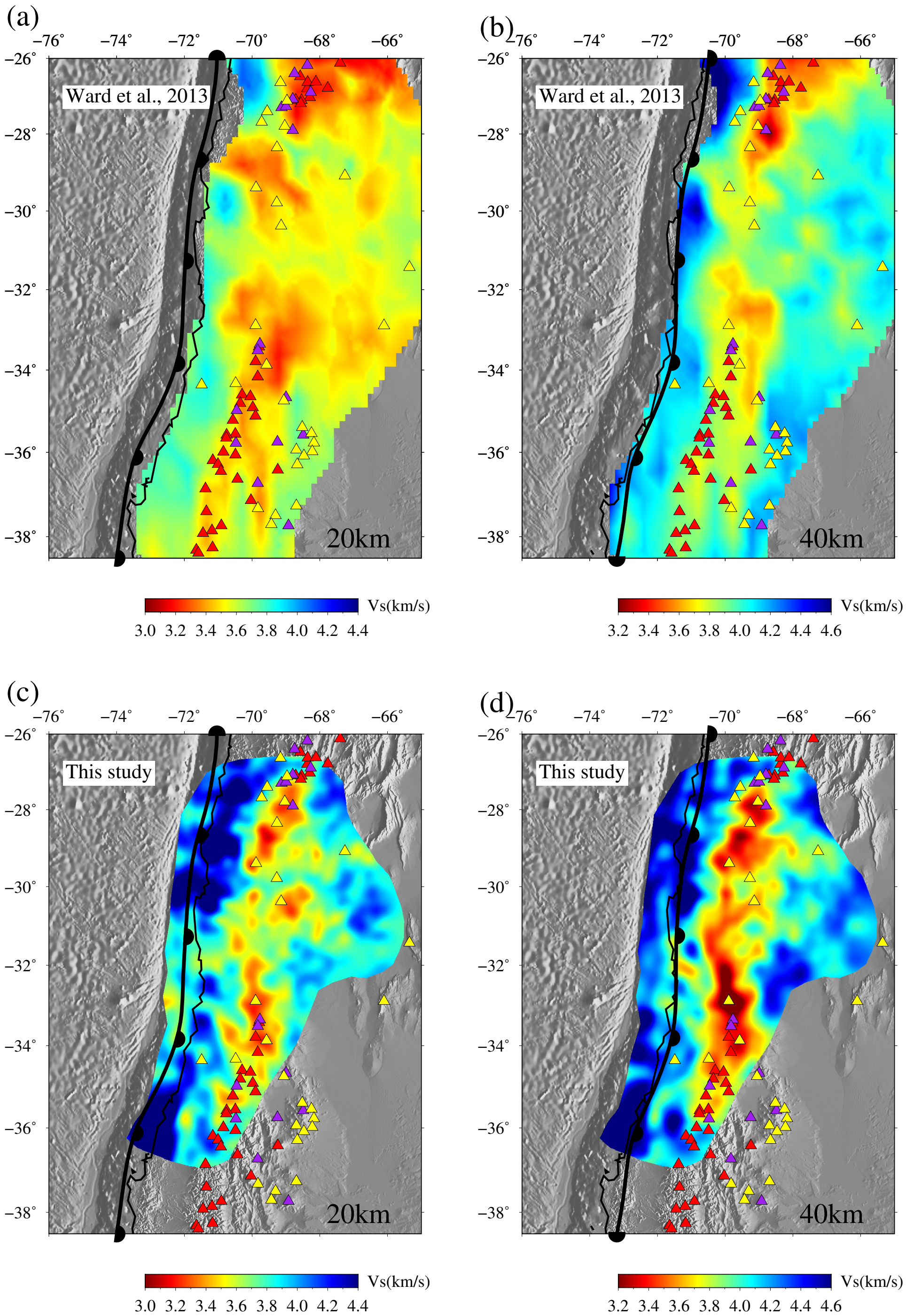

Figure S17. Comparison of the crustal structure inferred by the ambient noise tomography model of Ward et al. (2013) (top) with our model (bottom).

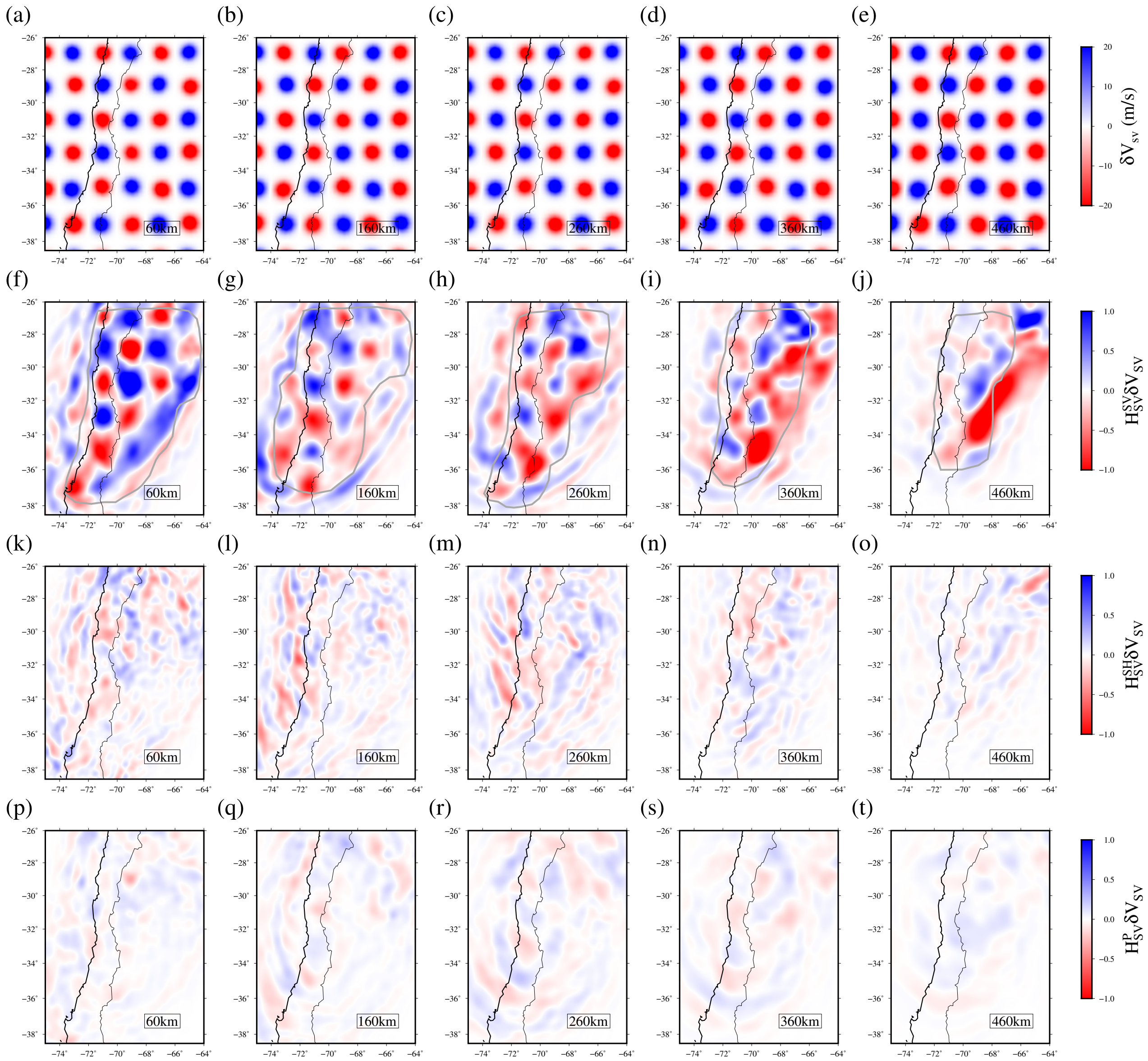

Figure S18. Point-spread function test with respect to $\mathbf{V}_{SV}$ perturbations ($\delta\mathbf{V}_{SV}$). (a-e): horizontal slices of input 1% Gaussian $\mathbf{V}_{SV}$ perturbations ($\delta\mathbf{V}_{SV}$) with σ=40 km at 60 km, 160 km, 260 km, 360 km and 460 km depth in the upper mantle; (f-j): point-spread functions $\mathbf{H}_{SV}^{SV}\delta\mathbf{V}_{SV}$ with respect to V_{SV} perturbations ($\delta\mathbf{V}_{SV}$) quantify the resolution for V_{SV}. (k-o): point-spread functions $\mathbf{H}_{SV}^{SH}\delta\mathbf{V}_{SV}$ quantify the cross-talk between V_{SV} and V_{SH}; (p-t) point-spread functions $\mathbf{H}_{SV}^{P}\delta\mathbf{V}_{SV}$ quantify the trade-off between V_{SV} and V_P. Gray thick lines in f-j denote the trust region for $\mathbf{V}_{SV}$ used for masking results plots.

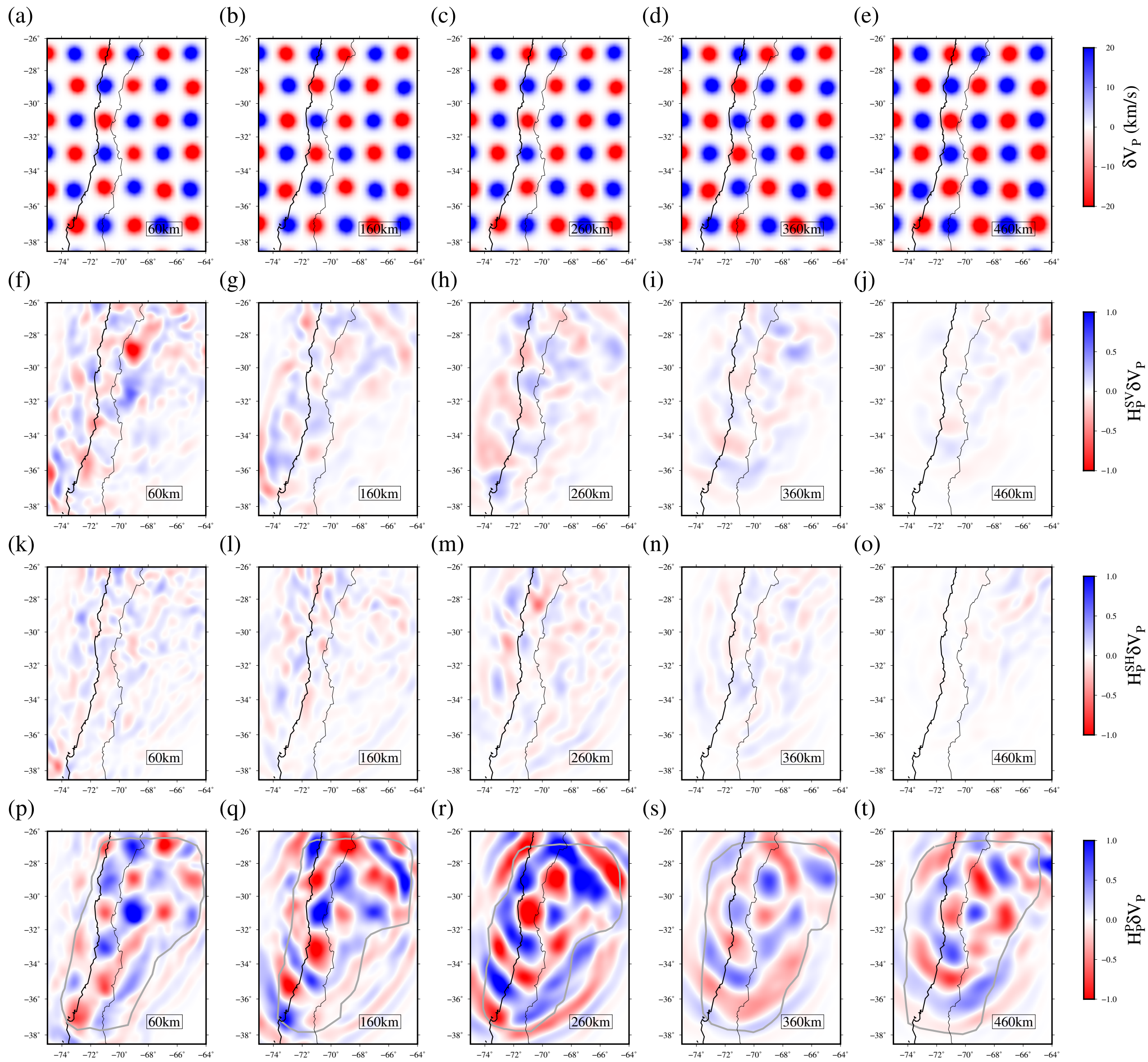

Figure S19. Point-spread function test with respect to isotropic $\mathbf{V}_P$ perturbations ($\delta\mathbf{V}_P$). (a-e): horizontal slices of input 1% Gaussian $\mathbf{V}_P$ perturbations ($\delta\mathbf{V}_P$) with σ=40 km at 60 km, 160 km, 260 km, 360 km and 460 km depth in the upper mantle; (f-j): point-spread functions $\mathbf{H}_P^{SV}\delta\mathbf{V}_P$ with respect to isotropic V_P perturbations ($\delta\mathbf{V}_P$); (k-o): point-spread functions $\mathbf{H}_P^{SH}\delta\mathbf{V}_P$; (p-t) point-spread functions $\mathbf{H}_P^{P}\delta\mathbf{V}_P$; Gray thick lines denote the trust region for $\mathbf{V}_P$.

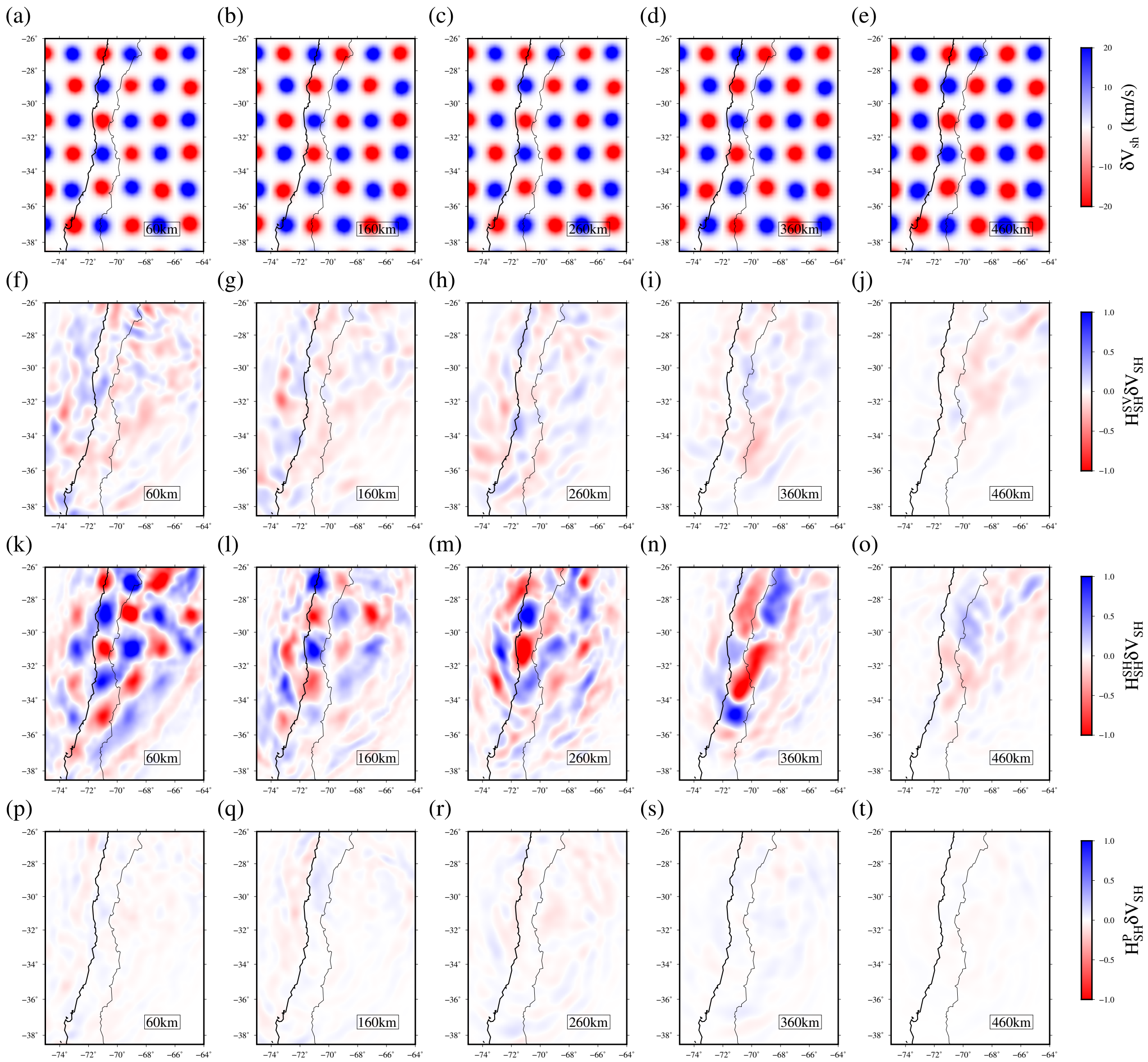

Figure S20. Point-spread function test with respect to $\mathbf{V}_{SH}$ perturbations ($\delta\mathbf{V}_{SH}$). (a-e): horizontal slices of input 1% Gaussian $\mathbf{V}_{SH}$ perturbations ($\delta\mathbf{V}_{SH}$) with σ=40 km at 60 km, 160 km, 260 km, 360 km and 460 km depth in the upper mantle; (f-j): point-spread functions $\mathbf{H}_{SH}^{SV}\delta\mathbf{V}_{SH}$ with respect to V_{SH} perturbations ($\delta\mathbf{V}_{SH}$); (k-o): point-spread functions $\mathbf{H}_{SH}^{SH}\delta\mathbf{V}_{SH}$; (p-t) point-spread functions $\mathbf{H}_{SH}^{P}\delta\mathbf{V}_{SH}$.

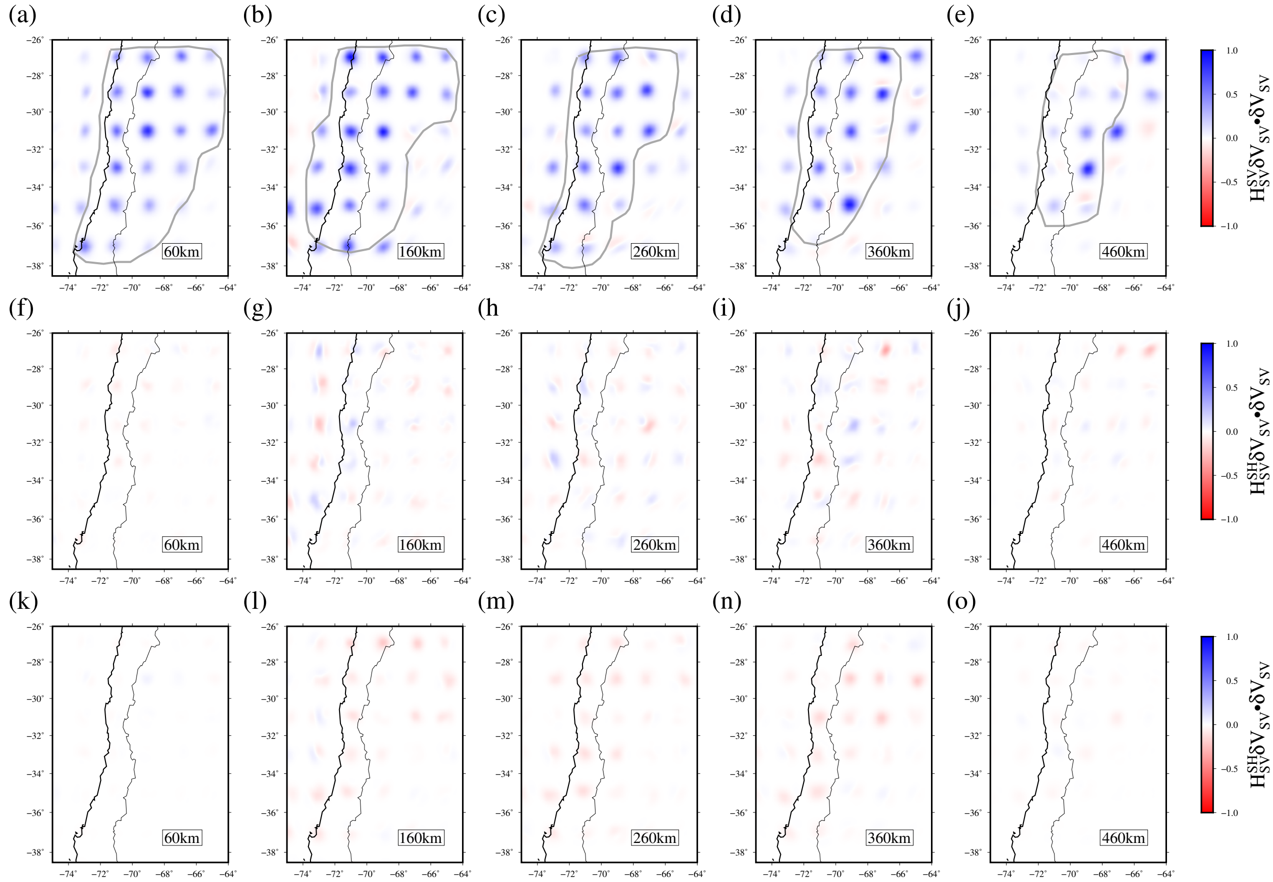

Figure S21. Normalised product between the $\delta\mathbf{V}_{SV}$ and point-spread functions $\mathbf{H}^{SV}_{SV}\delta\mathbf{V}_{SV}$ (a-e), $\mathbf{H}^{P}_{SV}\delta\mathbf{V}_{SV}$ (f-j) and $\mathbf{H}^{SH}_{SV}\delta\mathbf{V}_{SV}$ (k-o). All the results are normalised by the product of the maximum of $\delta\mathbf{V}_{SV}$ and the maximum of $\mathbf{H}^{SV}_{SV}\delta\mathbf{V}_{SV}$ for every depth level. The best resolution is indicated by blue dots of uniform amplitude for the same anomaly type (a-e); poor resolution by uneven recovery or red zones indicates failure to recover the basic anomalies. For perfect resolution the plots in f-o would be uniformly white; in fact minor cross-talk of parameters is observed. Note that this test focuses attention on recovery of correct anomaly polarities in the anomaly centres, giving a clearer picture in this regard than the raw checkerboard point spread recovery results, but that the importance of smearing effects is not visible. Both visualisations are therefore best considered together.

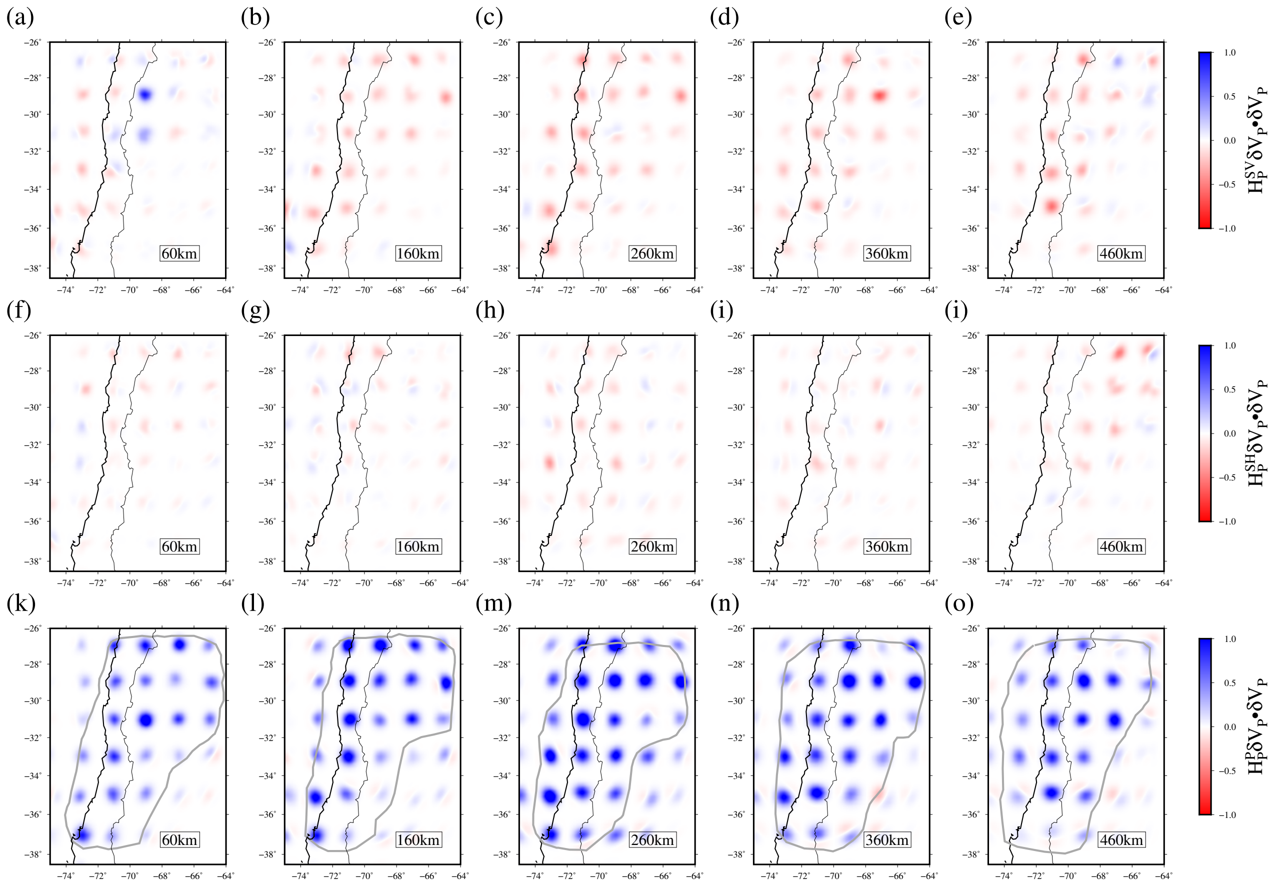

Figure S22. Normalised product between the $\delta\mathbf{V}_P$ and point-spread functions $\mathbf{H}_{SV}^{P}\delta\mathbf{V}_P$ (a-c), $\mathbf{H}_{P}^{SH}\delta\mathbf{V}_P$ (d-f) and $\mathbf{H}_{P}^{P}\delta\mathbf{V}_P$ (g-i). All the results are normalised by the product of the maximum of $\delta\mathbf{V}_P$ and the maximum of $\mathbf{H}_{P}^{P}\delta\mathbf{V}_P$ for every depth level.

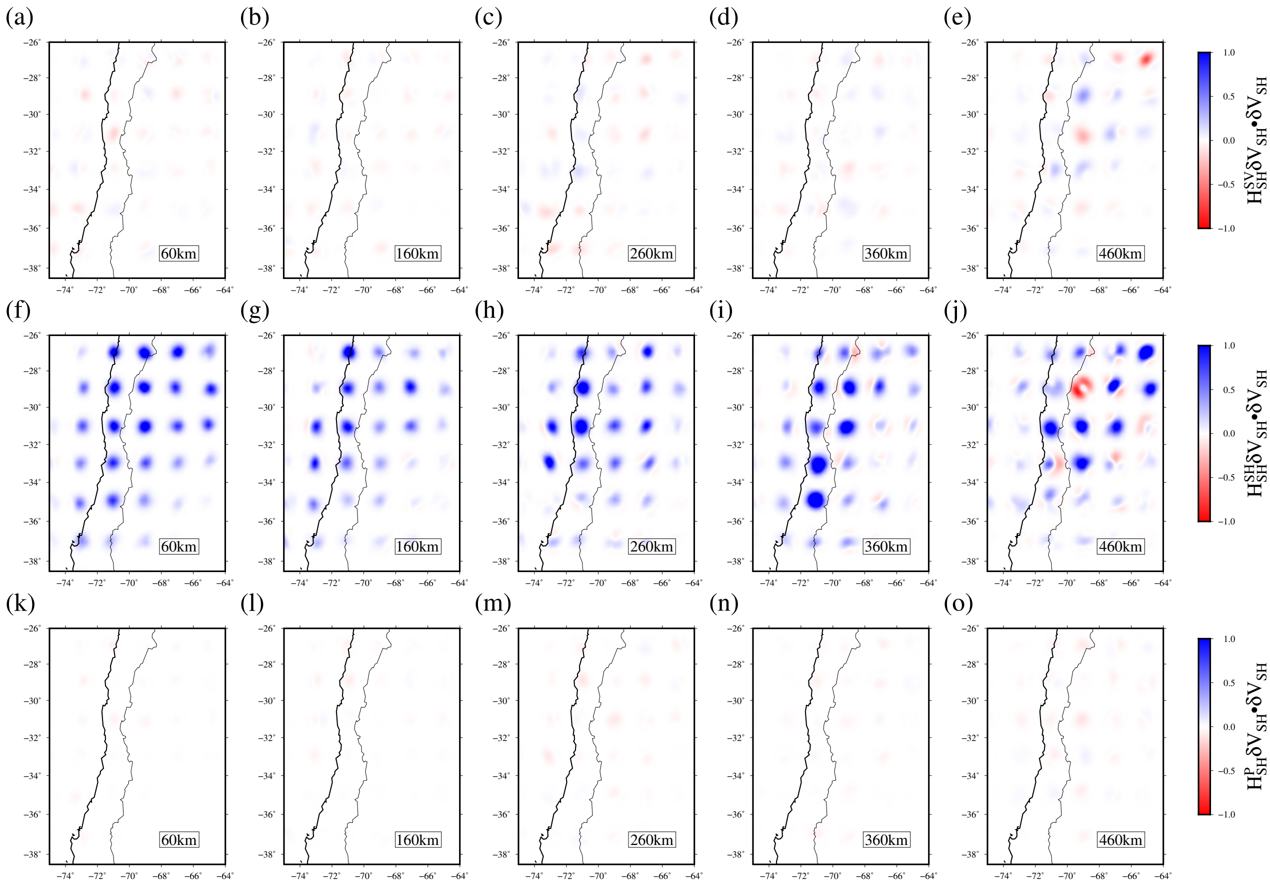

Figure S23. Normalised product between the $\delta\mathbf{V}_{SH}$ and point-spread functions $\mathbf{H}_{SV}^{SH}\delta\mathbf{V}_{SH}$ (a-c), $\mathbf{H}_{SH}^{SH}\delta\mathbf{V}_{SH}$ (d-f) and $\mathbf{H}_{P}^{SH}\delta\mathbf{V}_{SH}$ (g-i). All the results are normalised by the product of the maximum of $\delta\mathbf{V}_{SH}$ and the maximum of $\mathbf{H}_{SH}^{SH}\delta\mathbf{V}_{SH}$ for every depth level.

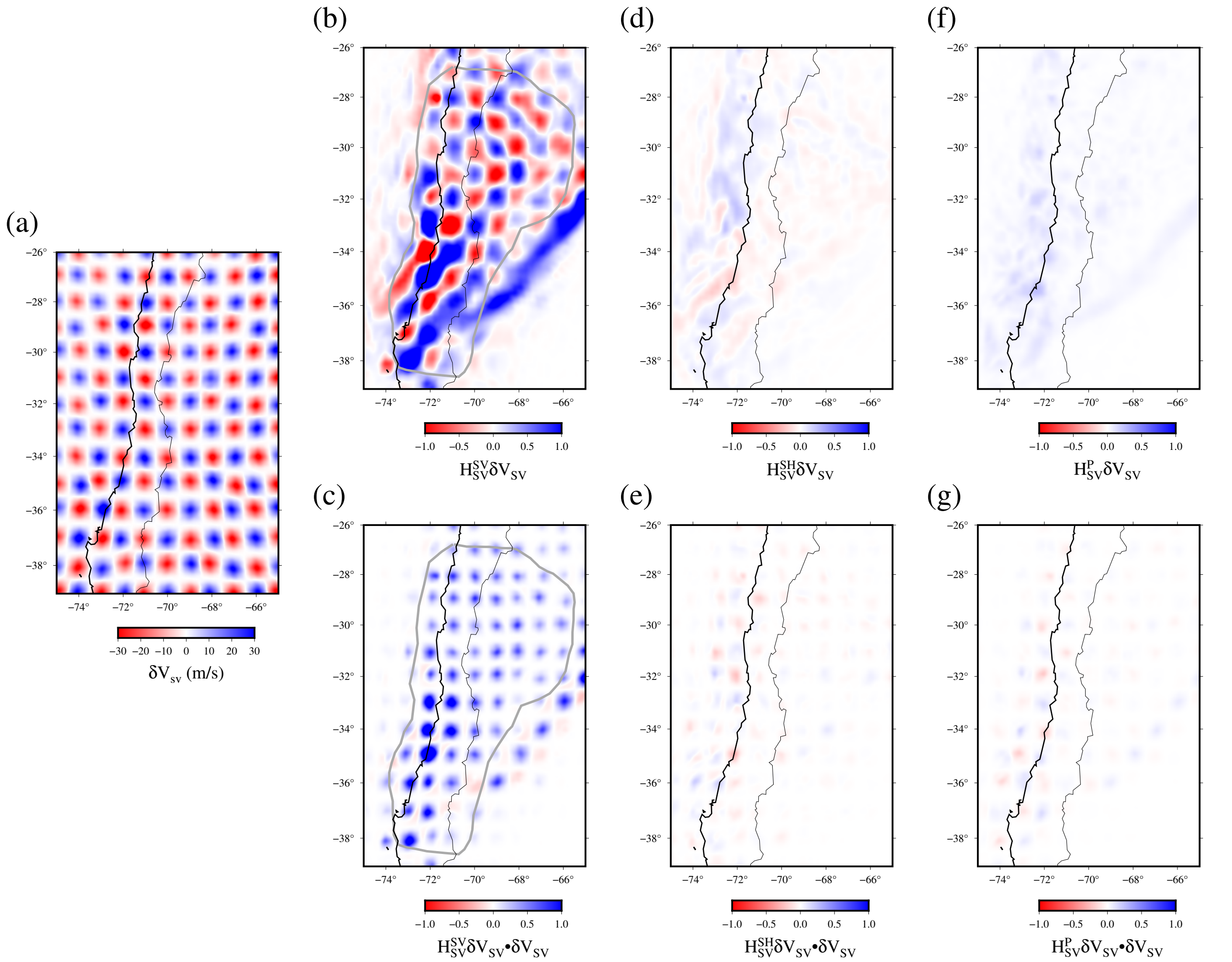

Figure S24. (a) Horizontal slice of input 1% Gaussian $\mathbf{V}_{SV}$ perturbations ($\delta\mathbf{V}_{SV}$) with σ=25 km at 20 km depth in the crust; (b), (d), (f) point-spread functions $\mathbf{H}_{SV}^{SV}\delta\mathbf{V}_{SV}$, $\mathbf{H}_{SV}^{SH}\delta\mathbf{V}_{SV}$, $\mathbf{H}_{SV}^{P}\delta\mathbf{V}_{SV}$ with respect to V_{SV} perturbations ($\delta\mathbf{V}_{SV}$), respectively. (c), (e), (g) Normalised product between the $\delta\mathbf{V}_{SV}$ and point-spread functions $\mathbf{H}_{SV}^{SV}\delta\mathbf{V}_{SV}$, $\mathbf{H}_{SV}^{SH}\delta\mathbf{V}_{SV}$, $\mathbf{H}_{SV}^{P}\delta\mathbf{V}_{SV}$, respectively. All the products are normalised by the product of the maximum of $\delta\mathbf{V}_{SV}$ and the maximum of $\mathbf{H}_{SV}^{SV}\delta\mathbf{V}_{SV}$

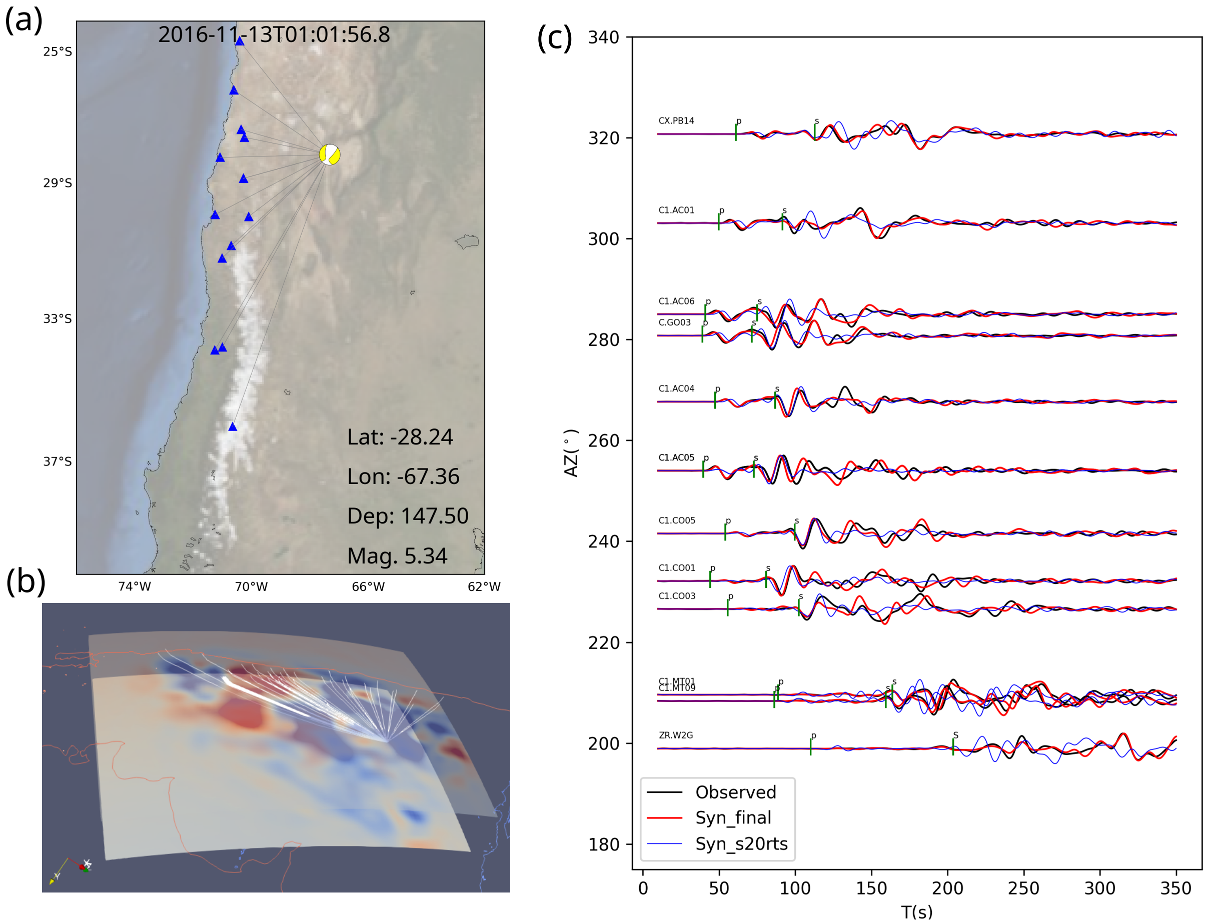

Figure S25. Waveform comparison between the initial and final model for Z component. (a) Map for example event (centroid depth 148 km) and stations. (b) 3D ray-path illustration. (c) Observed (black lines) and synthetic waveforms (blue: initial model - S20RTS; red: final model) for the indicated stations. Ray-path and arrival times are predicted for IASP91 using Taup toolkit in Obspy.

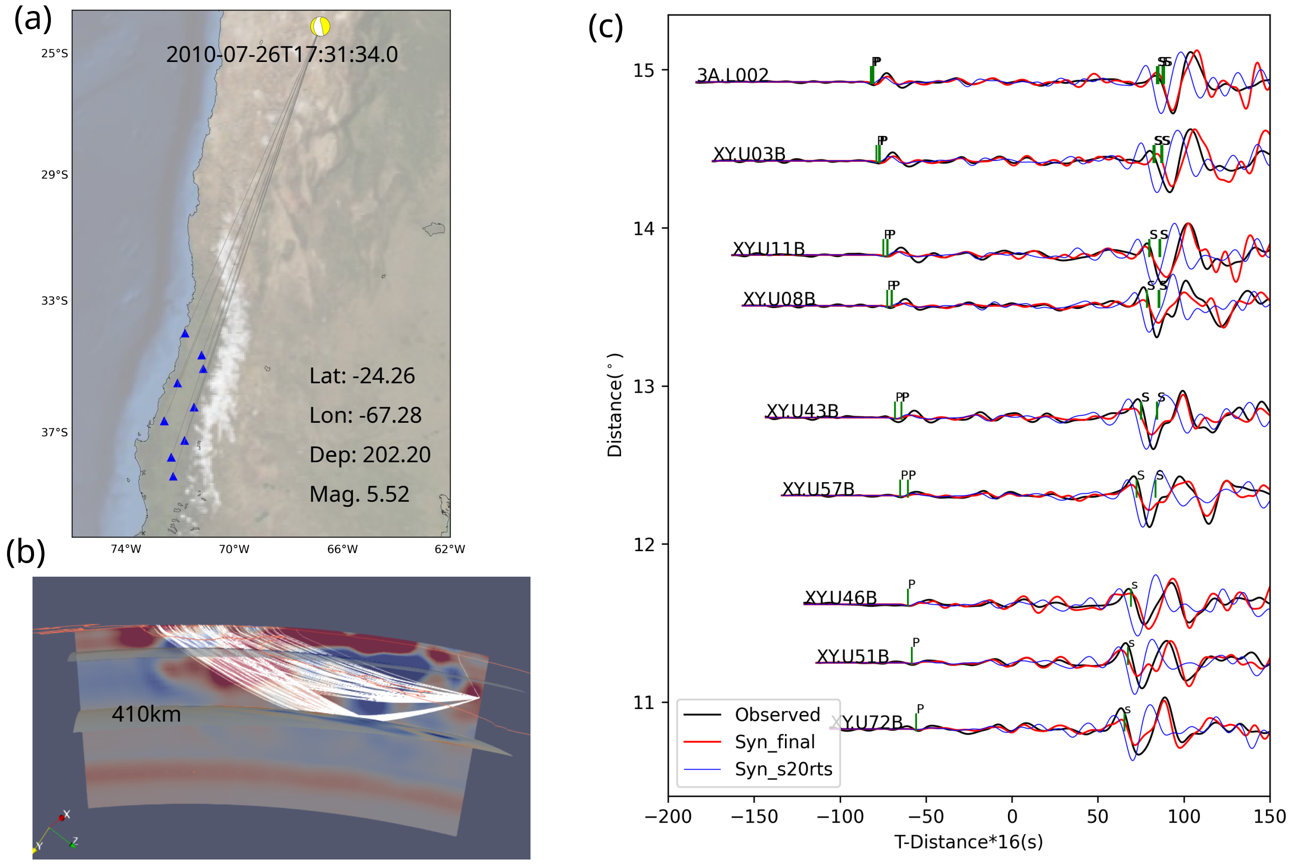

Figure S26. Waveform comparison for example event at centroid depth 202 km. For other figure elements see Fig. S25.

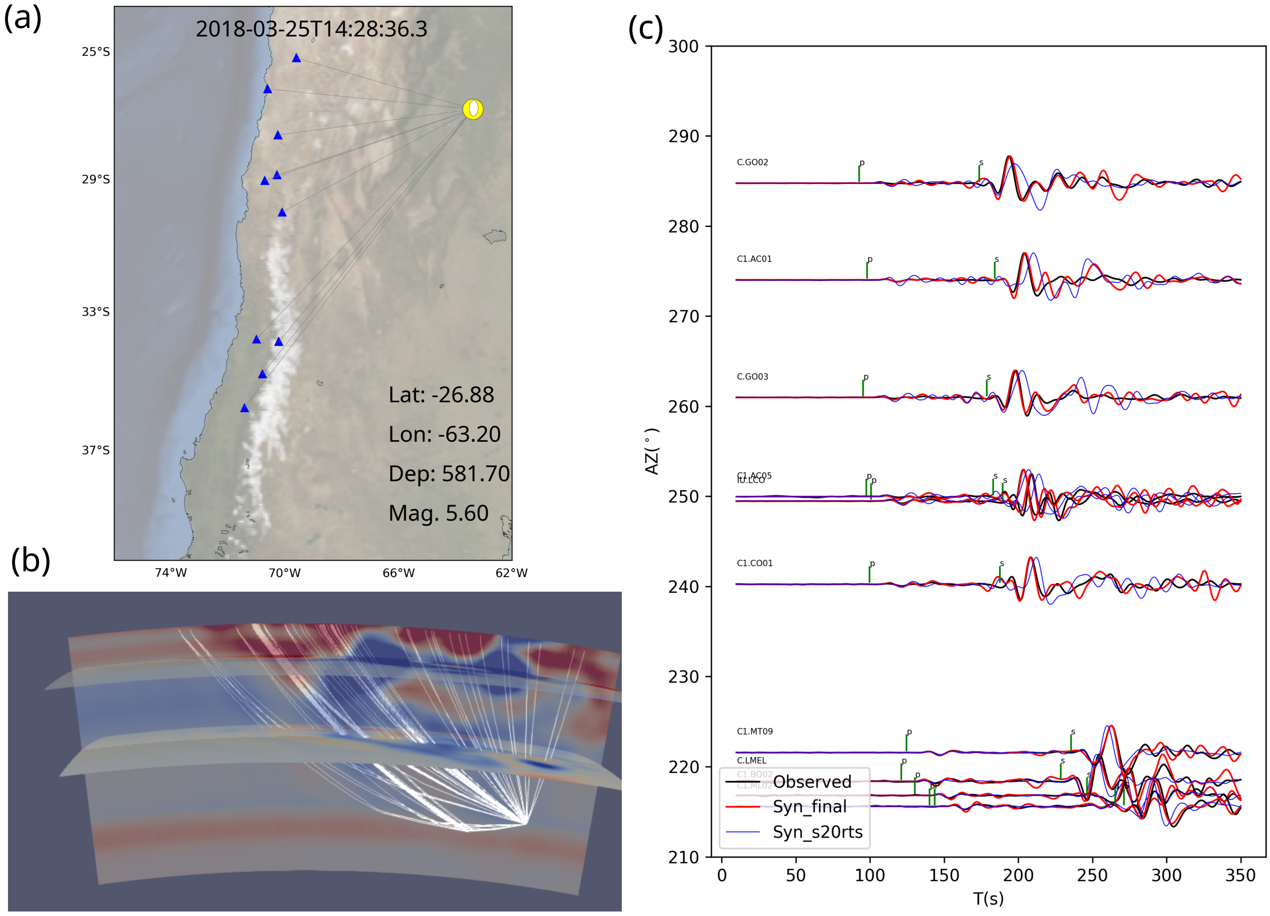

Figure S27. Waveform comparison for example event at centroid depth 582 km. For other figure elements see Fig. S25.

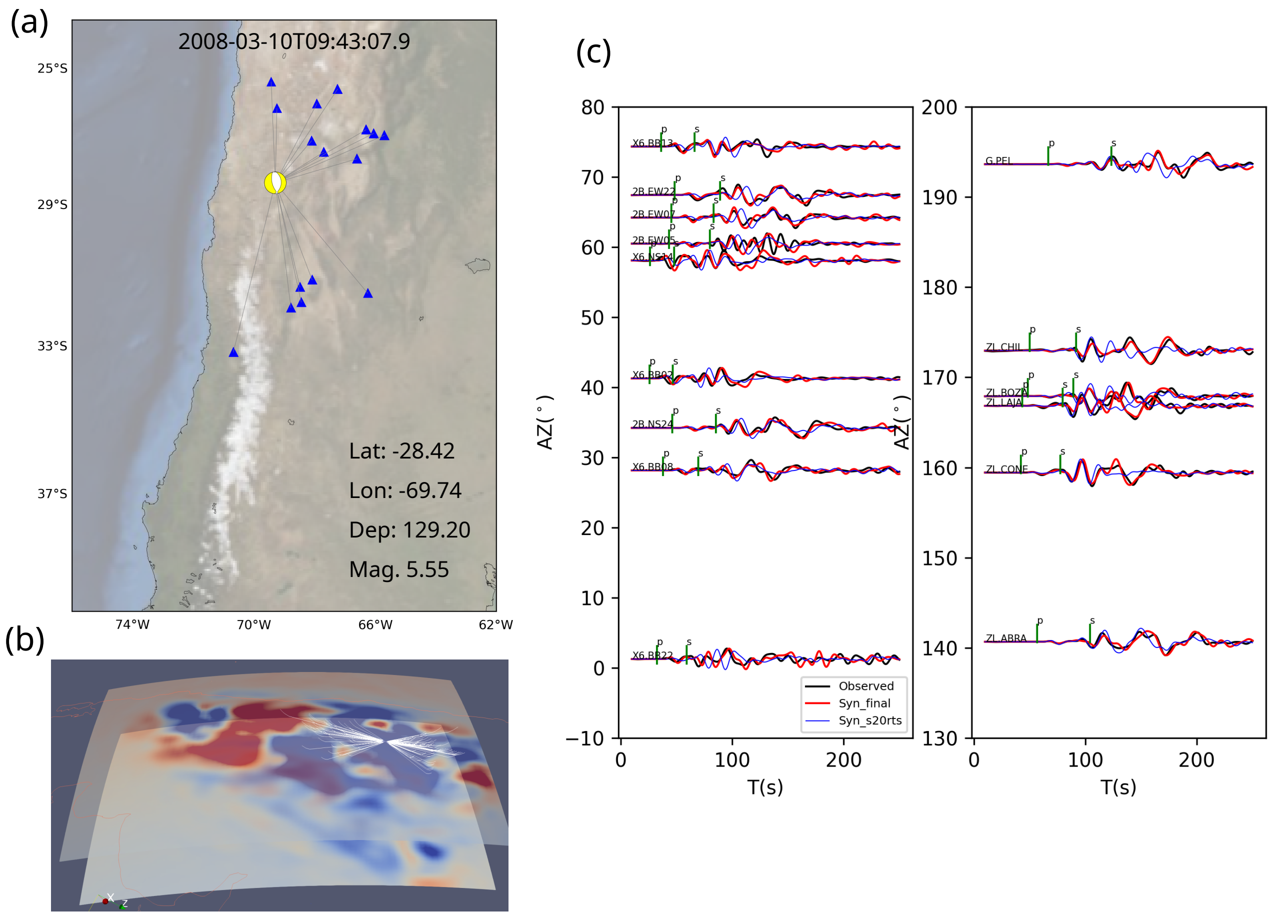

Figure S28. Waveform comparison for example event at centroid depth 129.20 km. For other figure elements see Fig. S25.